The Astrophysical Journal, 949:112 (18pp), 2023 June 1 https://doi.org/10.3847/1538-4357/acc465

The Impact of Multifluid Effects in the Solar Chromosphere on the Ponderomotive Force under SE and NEQ Ionization Conditions

Juan Martínez-Sykora[1,2,3,4], Bart De Pontieu[1,3,4], Viggo H. Hansteen[1,2,3,4], Paola Testa[5], Q. M. Wargnier[1,2], and Mikolaj Szydlarski[3,4]
[1] Lockheed Martin Solar & Astrophysics Laboratory, 3251 Hanover Street, Palo Alto, CA 94304, USA; juanms@lmsal.com
[2] Bay Area Environmental Research Institute, NASA Research Park, Moffett Field, CA 94035, USA
[3] Rosseland Center for Solar Physics, University of Oslo, P.O. Box 1029 Blindern, NO-0315 Oslo, Norway
[4] Institute of Theoretical Astrophysics, University of Oslo, P.O. Box 1029 Blindern, NO-0315 Oslo, Norway
[5] Harvard-Smithsonian Center for Astrophysics, 60 Garden Street, Cambridge, MA 02193, USA
Received 2022 November 29; revised 2023 February 13; accepted 2023 March 13; published 2023 June 2

Abstract

The ponderomotive force has been suggested to be the main mechanism to produce the so-called first ionization potential (FIP) effect—the enrichment of low-FIP elements observed in the outer solar atmosphere, in the solar wind, and in solar energetic events. It is well known that the ionization of these elements occurs within the chromosphere. Therefore, this phenomenon is intimately tied to the plasma state in the chromosphere and the corona. For this study, we combine IRIS observations, a single-fluid 2.5D radiative magnetohydrodynamics (MHD) model of the solar atmosphere, including ion–neutral interaction effects and nonequilibrium (NEQ) ionization effects, and a novel multifluid multispecies numerical model (based on the Ebysus code). Nonthermal velocities of Si IV measured from IRIS spectra can provide an upper limit for the strength of any high-frequency Alfvén waves. With the single-fluid model, we investigate the possible impact of NEQ ionization within the region where the FIP may occur, as well as the plasma properties in those regions. These models suggest that regions with strongly enhanced network and type II spicules are possible sites of large ponderomotive forces. We use the plasma properties of the single-fluid MHD model and the IRIS observations to initialize our multifluid models to investigate the multifluid effects on the ponderomotive force associated with Alfvén waves. Our multifluid analysis reveals that collisions and NEQ ionization effects dramatically impact the behavior of the ponderomotive force in the chromosphere, and existing theories may need to be revisited.

Unified Astronomy Thesaurus concepts: Solar atmosphere (1477); Solar corona (1483); Solar abundances (1474); Stellar coronae (305); Solar chromosphere (1479); Stellar physics (1621); Stellar atmospheres (1584); Solar spicules (1525); Solar magnetic fields (1503)

1. Introduction

The chromosphere is a highly complex, finely structured, and dynamic region in which non-LTE radiative transfer and time-dependent ionization play a major role. In the chromosphere, high-FIP elements remain neutral, while low-FIP elements are ionized. It is here that chemical fractionation in the solar atmosphere must begin. Observations suggest that neutral elements remain well mixed with hydrogen, while ionized elements are preferentially pushed upward (Meyer 1985; Feldman 1992; Testa 2010; Testa et al. 2015). Other stars also exhibit fractionation effects in their coronal composition compared with photospheric abundances, and their coronal chemical composition shows some dependence on the stellar activity level (see reviews by Testa 2010; Testa et al. 2015, and references therein). To further understand this process, one should keep in mind that the chromosphere is highly dynamic due to the presence of shocks and magnetic field dynamics (e.g., Carlsson & Stein 1992). In such a dynamic and highly structured chromosphere, ionization shows strong gradients (of many orders of magnitude) and is not in LTE nor in statistical equilibrium. Due to the long recombination timescale of hydrogen and helium in the chromosphere, the ionization depends on the history of the plasma (Leenaarts et al. 2007; Golding et al. 2016; Martínez-Sykora et al. 2020; Przybylski et al. 2022). This means that ion–neutral collision frequencies vary by many orders of magnitude on small scales within the solar atmosphere (e.g., Martínez-Gómez et al. 2015; Martínez-Sykora et al. 2020; Nóbrega-Siverio et al. 2020; Khomenko et al. 2021; Rempel & Przybylski 2021; Wargnier et al. 2022).

The chemical composition of the solar wind is also an indicator of the source region on the Sun (Geiss et al. 1995) and is critical to establishing the magnetic connectivity from the wind to the surface. A well-known example corresponds to in situ measurements of helium abundances at 1 au that depend on the solar wind speed and phase of the activity cycle (Kasper et al. 2012). The smallest helium abundances are observed during solar minimum. These dependencies point to mechanisms that affect the second-most abundant constituent of the solar corona and whose effectiveness changes depending on the levels of activity on the Sun. Similarly, Landi & Testa (2015) have found the coronal Ne/O abundance ratio varies by more than a factor of two during the solar cycle and peaks at the cycle minimum. The new NASA mission Parker Solar Probe (PSP; Fox et al. 2016) and the Solar Orbiter (SO; Müller et al. 2020) approach our star and measure the fields and particles much closer than 1 au, where the plasma is less evolved and still preserves many of the original properties (composition, charge, kinetic properties, etc.) of the near surface. However,

establishing direct links to the surface (observed with remote sensing instruments) remains a major challenge. One of the most striking recent discoveries by PSP is the Alfvénic magnetic field reversals known as switchbacks in the inner heliosphere (Bale et al. 2021). The structures appear to be separated on spatial scales associated with the supergranular scales. Therefore, it is thought that these structures originate at the base of the lower solar atmosphere. A possible mechanism to drive the switchbacks is interchange reconnection in the lower corona (Bale et al. 2022). However, the switchbacks are also linked with the enrichment of alpha particles, depletion of electron temperature, and slow solar wind (Fargette et al. 2021; Woolley et al. 2021). The chemical fractionation, as well as the origin of the enhancement of alpha particles, should occur in or close to the chromosphere, where plasma is partially ionized, suggesting the driving mechanism of these phenomena may be connected to this region. Studies such as these highlight the challenges and opportunities of establishing the connectivity between the solar surface and the solar wind. This is important also because understanding the connectivity between stellar surfaces and their winds, the connection to the drivers, and their impact on the heliosphere and astrospheres, is key to predicting space weather.

The ponderomotive force associated with strong Alfvén waves is currently regarded as the most likely mechanism to explain the FIP effect as modeled for instance by Laming (2004, 2015). Nonetheless, this model uses a simplified approach based on 1D semi-empirical, static atmospheres from Avrett (2007). While these models can treat the radiation in NLTE, i.e., including collisional and photoionization, radiative, three-body, and/or dielectronic recombination, these atmospheric models estimate the ionization state from averaged observations or assuming statistical equilibrium (SE). Such semi-empirical models do not capture the complex dynamics of the chromosphere, and as such, they are not a good test bed for wave propagation and fractionation studies. Under those assumptions, and in order to reproduce the observables in most solar targets, the model prefers Alfvén waves that are generated in the corona and that propagate (from above) into the chromosphere where they are reflected. This theory postulates that nanoflares and reconnection in the coronal volume drive the downward-propagating Alfvén waves.

Observational evidence for low-frequency Alfvén waves shows a predominance of upward-propagating Alfvén waves in the chromosphere (e.g., De Pontieu et al. 2007; Okamoto & De Pontieu 2011). Similarly, observations in the corona indicate a predominance of upward-propagating Alfvén waves (Tomczyk et al. 2007; McIntosh et al. 2011) or a mix of upward and downward waves in which the upward flux exceeds the downward flux by a significant factor (McIntosh & De Pontieu 2009). It is, of course, possible that high-frequency Alfvén waves, which are much more difficult to detect, due to observational limitations, somehow show significantly different behavior.

Damping of Alfvén waves occurs due to ion–neutral interactions, and hence Pedersen resistivity (ambipolar diffusion) can be significant in the chromosphere (e.g., De Pontieu et al. 2001; Ballester et al. 2018). This damping could be enhanced by the interaction between different species (e.g., Zaqarashvili et al. 2011; Popescu Braileanu et al. 2019; Martínez-Sykora et al. 2020). Another possible dissipation mechanism is the transverse wave-induced Kelvin–Helmholtz rolls predicted by the KHI-resonant absorption (Soler et al. 2012; Antolin et al. 2018). Those dissipation mechanisms could play a role in heating the chromosphere and change the wave power throughout the chromosphere. In the corona, the impact of multifluid effects on high-frequency Alfvén waves has been investigated by, e.g., Ofman et al. (2005) and Maneva et al. (2015), where anisotropies in the wave and heating seem to occur.

Dahlburg et al. (2016) computed the ponderomotive acceleration from a 3D MHD model outer solar atmosphere, including optically thin radiation and thermal conduction. This ponderomotive acceleration in the model occurs at the footpoints of coronal loops as a byproduct of wave-driven coronal heating. The first part of this present work broadly extends this study on the ponderomotive force in realistic radiative MHD simulations, which include nonequilibrium ionization effects, ion–neutral interaction effects, and a better description of chromospheric radiative losses (Section 4).

In the following, the theory behind the ponderomotive force is briefly described in Section 2. In Section 3, we describe how we use IRIS observations to estimate an upper limit to the amplitude of high-frequency Alfvén waves (Section 3). As mentioned, the results regarding the characterization of the ponderomotive force in the radiative MHD model under SE and NEQ conditions are described in Section 4. We then present the multifluid models where we investigate the collisional effects on the ponderomotive acceleration for Alfvén waves (Section 5). Finally, the manuscript ends with our conclusions and a discussion (Section 6).

2. Theoretical Considerations Regarding the Ponderomotive Force

The Lorentz force is a key force for understanding the dynamics of plasmas. It is a straightforward term that acts on charged particles. However, it is not always practical to use this term in complex scenarios, such as when electromagnetic waves or complex environments are involved. For such conditions, the ponderomotive force is often used to simplify understanding of the plasma dynamics. The ponderomotive force is based on the time average of nonlinear forces that act in the presence of oscillating electromagnetic fields. However, the calculation of this force is rather cumbersome because it includes nonlinear aspects, and it usually involves quite limiting assumptions, rendering the results approximate. There are a variety of formulations of the ponderomotive force, which differ in the underlying assumptions. All variations of the ponderomotive force are derived by a nonlinear dependence on the amplitude of the electric field oscillations. This force can be treated as the acceleration in a electron-ion plasma, or in ions, as nicely described in Whitelam et al. (2002). They described the acceleration along the magnetic field associated with the ponderomotive force resulting from nonlinear propagation of circularly polarized electromagnetic (CPEM) waves in an electron-ion plasma as follows:

$$F = -\left(\frac{\partial}{\partial z} + \frac{k\Omega_{cj}}{\omega(\omega+\Omega_{cj})}\frac{\partial}{\partial t}\right)\frac{q_j^2|\boldsymbol{E}|^2}{m_j\omega(\omega+\Omega_{cj})}, \quad (1)$$

where $\boldsymbol{E}$ is the electric field; ω and k are the wave frequency and number, respectively; and Ω_{cj}, m_j, and q_j are the gyrofrequency, mass, and charge for species j (j can be any ionized species or electrons). Whitelam et al. (2002) also

considered a case in which the ion acceleration is produced by electromagnetic electron-cyclotron (EMEC) or ion-cyclotron Alfvén (EMICA) waves, in which they assumed that the ponderomotive force dominates over the background Lorentz force and pressure gradients:

$$F = -\frac{q_i^2}{m_e\omega(\omega - |\Omega_{ce}|)}\left(\frac{\partial}{\partial z} - \frac{k\Omega_{ce}}{\omega(\omega - |\Omega_{ce}|)}\frac{\partial}{\partial t}\right)|\boldsymbol{E}|^2 . \quad (2)$$

For the case of a multi-ion species and the ponderomotive force from EMICA waves, the α species is governed by

$$F = -\frac{m_i q_{i\alpha}^2}{m_{i\alpha}^2\Omega_{ci\alpha}}\left[\frac{1}{\omega - \Omega_{ci\alpha}}\frac{\partial}{\partial z} + \frac{k}{\omega^2}\left(1 - \frac{\Omega_{ci\alpha}^2}{(\omega - \Omega_{ci\alpha})^2}\right)\frac{\partial}{\partial t}\right]|\boldsymbol{E}|^2 . \quad (3)$$

It should be noted that the spatial and temporal components considered in the literature are sometimes treated as different forces. A nice summary of the various calculations of different forces can be found in Lundin & Guglielmi (2006). In short, we list a few relevant items from that paper:

1. Lundin–Hultqvist force or magnetic moment pumping (MMP) is given by

$$F = -\frac{mc^2}{2}\frac{E^2}{B^2}\nabla_{||}\ln B \quad (4)$$

(Lundin & Hultqvist 1989). Here, $\boldsymbol{B}$ is the magnetic field. This ponderomotive force assumes a low-frequency regime, that the electric field oscillation is perpendicular to the magnetic field, and a very slow variability in B. This force is always oriented in the direction of decreasing B (independent of the wave propagation direction).

2. Miller force or gradient ponderomotive force

$$F = \frac{mc^2}{4B^2}\frac{\partial E^2}{\partial z} \quad (5)$$

This force is related to the spatial inhomogeneity of the wave field. The derivation of the force assumes a static magnetic field with a perpendicular oscillation between the electric field and magnetic field, where the magnetic field perturbations are negligible compared to the ambient magnetic field. The formula provided is for Alfvén waves with low frequency. This force is positive (in the direction of wave propagation) if the gradient of the wave field is positive (i.e., increasing in the direction of wave propagation).

3. The Abraham force is

$$F = \pm\frac{mc^2}{2v_A B^2}\frac{\partial E^2}{\partial t}. \quad (6)$$

This description of the ponderomotive force neglects standing waves and applies to waves traveling parallel to the magnetic field. The positive (negative) sign corresponds to a wave propagating in the direction (opposite that) of the magnetic field.

It should be noted that Laming (2015) uses a combination of the Lundin–Hultqvist and Miller forces, and this force is for the plasma ions due to wave refraction.

The chromosphere is partially ionized, and none of these studies consider the ponderomotive effects of damping of Alfvén waves from ion–neutral interactions. Haerendel (1992) takes into account the presence of collisions, and the ponderomotive force has a very different dependence:

$$F = \rho_n u_x^2 \frac{\omega^2}{2v_A\nu_{ni}} , \quad (7)$$

where ρ_n and ν_{ni} are the neutral density and collision frequency between ions and neutrals, respectively. v_A is the Alfvén speed. We note that this force is a factor of two smaller than originally reported by Haerendel (1992). The corrected formula is provided in De Pontieu & Haerendel (1998). This formula is based on the WKB approximation of a weakly damped wave and is averaged over a wave period. A derivation for strongly damped waves is provided by Song & Vasyliūnas (2011). The nature of this force is such that it is proportional to the damping of the wave field along the direction of propagation, i.e., $F \sim -\frac{\partial E^2}{\partial z}$. It should also be noted that the frequency dependence is different from Equation (1), which decreases with increasing frequency. The ion–neutral damping of the waves leads to a damping length L for the wave field:

$$L = \frac{2v_A\nu_{ni}\rho_t}{\omega^2\rho_n} , \quad (8)$$

where ρ_t is the total mass density and ρ_n is the neutral mass density.

As we will show with our multifluid models (Section 5.3), the many assumptions underlying some of these equations are not necessarily easy to justify for solar conditions or even the simplified scenarios we consider here (no density stratification or dynamics, and only Alfvén waves in the low-frequency regime).

3. IRIS Observations: Nonthermal Velocity

We have selected a decaying AR with plage and a large presence of spicules near the limb to characterize the high-frequency Alfvén waves traveling along the spicules, which will be used to constrain our models in the following sections. The exposure time of the selected IRIS observation is sufficient to set constraints on high-frequency waves, i.e., as short as possible (see below for details).

3.1. Target and Data Calibration

For this study, we use IRIS observations acquired from 2014 December 11 22:39:14 to 23:32:274 in a plage region near the limb $(x, y) = (-910'', -233'')$. IRIS observed this active region (AR) with a very large, sparse 64-step raster, with no roll, exposures of 2 s, a cadence of 3.2 s, raster scans of 199 s, and 2x2 binning (i.e., a spatial plate scale of $0.''33$ and spectral sampling of 5.4 km s^{-1}), using OBSID 3820105390. The observation includes 14 full rasters. This study focuses only on the 13th raster, which is free of radiation hits from passage through the South Atlantic Anomaly (SAA). The slit-jaw image (SJI) data are obtained in the 1330 and 2796 passbands. We use IRIS calibrated level 2 data, which have been processed for dark current, flat field, and geometrical corrections (De Pontieu et al. 2014).

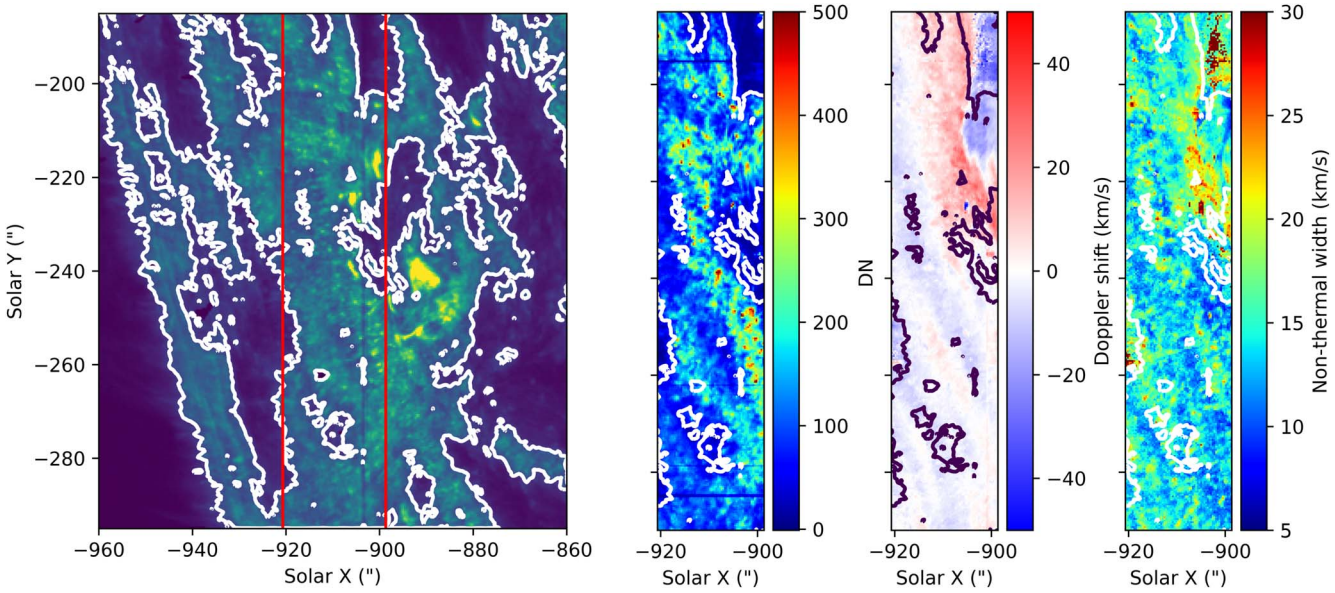

Figure 1. From left to right, IRIS SJI 1330 at 23:28:32, and the total intensity, Doppler shift, and nonthermal width from Si IV 1339 Å from fitting a single Gaussian. The contours correspond to the SJI 1330 at 100 DN. The vertical red lines in the left panel limit the region of the raster scan.

3.2. Analysis of the IRIS Observations

We fit Si IV 1339 Å profiles with a single Gaussian to extract the Doppler shifts and nonthermal widths (see Figure 1). The nonthermal velocity ($u_{\rm noth}$) is determined from the $1/e$ width of the single Gaussian fit (σ_e) by taking the square of the $1/e$ width after subtracting the squares of the instrumental ($\sigma_{\rm instr}$) and thermal ($\sigma_{\rm th}$) contributions ($u_{\rm noth} = \sqrt{\sigma_e^2 - \sigma_{\rm instr}^2 - \sigma_{\rm th}^2}$) (see Testa et al. 2016). Because the observation is near the limb, the nonthermal width contains mostly unresolved velocities that are expected to be almost perpendicular to the magnetic field. One can recognize spicules and moss in the SJI and Si IV line intensity map (left two panels). In plage and spicules, most nonthermal velocities range from 10 to 25 km s^{-1}. The exposure time is 2 s, so the assumption that the unresolved velocity comes from Alfvén waves suggests that they may have high frequencies (1 s or smaller) with amplitudes within [15, 36] km s^{-1}. We note that there is also plentiful observational evidence for Alfvén waves at lower frequencies (De Pontieu et al. 2007; Tomczyk et al. 2007; McIntosh et al. 2011; Okamoto & De Pontieu 2011).

4. Characterizing the Ponderomotive Acceleration and Chemical Fractionation in rMHD Simulation: SE versus NEQ

This section briefly describes the single-fluid radiative MHD numerical model and plasma properties in the simulated chromosphere, including the ponderomotive force (calculated after the simulation was run), to understand the conditions under which an FIP effect could possibly occur.

4.1. Radiative MHD Numerical Model Including NEQ Ionization and Ambipolar Diffusion

For the forward analysis, we used an already analyzed radiative MHD model computed with Bifrost (Gudiksen et al. 2011), which includes nonequilibrium ionization for hydrogen and helium (Leenaarts et al. 2007; Golding et al. 2016) as well as ambipolar diffusion (Nóbrega-Siverio et al. 2020). In short, this 2.5D numerical model mimics two plage regions connected by ∼40 Mm long loops and reveals features resembling type I and II spicules, low-lying loops, and other features. The simulation spans a vertical domain stretching from ∼3 Mm below the photosphere to 40 Mm above into the corona, with a nonuniform vertical grid size of 12 km in the photosphere and chromosphere and 14 km grid size in the horizontal axis. For further details about the numerical model, we refer to Martínez-Sykora et al. (2020). We have chosen this model because it includes NEQ effects and produces type II spicules and the associated Alfvén waves (Martínez-Sykora et al. 2017).

4.2. Characterizing the Simulated Chromospheric Properties for the Chemical Fractionation

In this numerical model, we computed the ionization fraction for various species with both low (calcium, iron, and silicon) and high (hydrogen and helium) FIP (Figure 2). We derive from the model the ionization fraction for hydrogen and helium in SE (panels (a) and (b)) as well as in NEQ ionization (panels (c) and (d)). We assumed photospheric abundances (Asplund et al. 2009, consistent with the underlying MHD model), and statistical and thermal equilibrium for the ionization and density populations for neutrals and ions in the SE cases. Low-FIP species, e.g., calcium, iron, and silicon, are highly ionized in a large fraction of the chromosphere in SE, whereas high-FIP species, including hydrogen and helium, are mostly neutral in the chromosphere in SE. However, NEQ ionization effects significantly increase the ionization fraction for hydrogen (panel (c)) and helium (panel (d)) and lead to a larger height range where these species are partially ionized (Leenaarts et al. 2007; Golding et al. 2016).

A comparison between hydrogen ionization fraction and any other species ionization fraction allows us to visualize the region of interest where the first ionization occurs for the various species (for low and high FIP) and chemical fractionation may occur. Figure 3 shows the ratio of hydrogen ionization fraction with the ionization fraction of any other species. We considered this comparison in SE (left column)

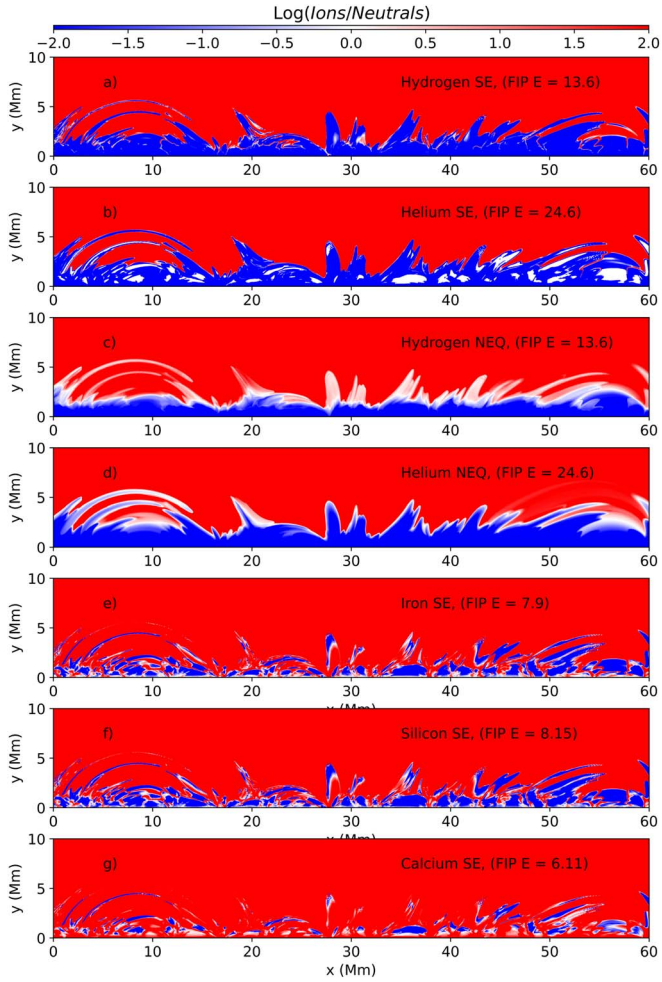

Figure 2. Ionization fractions are shown for various species with low and high FIP (hydrogen in panels (a) and (c), helium in panels (b) and (d), iron in panel (e), silicon in panel (f), and calcium in panel (g)). Panels (a) and (b) assume SE, and panels (c) and (d) are in NEQ for hydrogen and helium. Color bar is in log-scale. Labels in the panels show the FIP energy in eV.

and NEQ ionization for hydrogen and helium (right column). The red or blue regions are regions of interest in terms of fractionation, because the ionization degree between low- and high-FIP elements is significantly different (either higher or lower, respectively) in these regions. If a physical process like the ponderomotive force were to act in these regions, it would potentially lead to relative enrichment (or depletion) of elements with different FIP. In addition, in NEQ, the ionization degree may be inverted in extended areas (red color), i.e., the hydrogen is ionized when the other species are neutral, e.g., panels (d), (f), and (h)). We note that, in NEQ, there are a few regions, e.g., $x = [52, 57]$ Mm, where the helium ionization rate is higher than the hydrogen ionization rate. This results from having some remnant alpha particles from previously very hot low-lying loops, and alpha particles can take a very long time to recombine.

However, we note that, to have chemical fractionation, a different degree of ionization between the various species is not sufficient, because: (1) a physical process needs to act on the various species (e.g., ponderomotive force) to accelerate the particles upward and (2) the dynamics of the various species need to be somewhat decoupled from the timescales involved in the acceleration (i.e., collisions between high- and low-FIP elements cannot dominate, because these can couple the dynamics of the various elements). We compute the collisional rates between hydrogen, which is the most abundant fluid and will provide a good estimate of coupling, and other ionized species, again considering SE (left) and NEQ (right), in Figure 4. The upper chromosphere and transition region are weakly collisional. A weakly collisional region is where collisional timescales are a significant fraction of the wave period. Therefore, we define as weakly collisional the regions where collision frequencies are lower than 10 Hz, and the driver of the chemical fractionation may occur in those locations. It should be noted that, in the simulation, the collision frequencies for ionized iron, silicon, and calcium are the same in NEQ and SE because they do not depend on hydrogen number density. Their contribution to the momentum exchange nevertheless depends on the hydrogen number density (e.g., see Wargnier et al. 2022).

A key aspect is where in the model the assumed physical process (ponderomotive force) is likely to be important. Dahlburg et al. (2016) estimated the ponderomotive acceleration in their 3D model, considering the perturbations of the perpendicular component of the electric field along the magnetic field. Similarly, we compute the electric field perturbation along the magnetic field as follows:

$$\delta_s E = \frac{1}{B^2}\frac{\partial E^2}{\partial s}, \tag{9}$$

where s is along the loop. We mask regions with high collision rates ($\geqslant$10 Hz) for each element as well as regions where they have the same ionization state as hydrogen (Figure 5). By masking out these regions, we get the region of interest (the nonmasked region), where the action of $|\delta_s E|$ may lead to chemical fractionation for each species. Different structures show different $|\delta_s E|$, with type II spicules experiencing the largest values. It should be noted that the region of interest changes depending on which species are considered. Those masks reveal the complexity of this problem, due to the highly structured and dynamic atmosphere.

Since the models in Dahlburg et al. (2016) were driven by waves, expression 9 estimates the ponderomotive acceleration. This is not necessarily true in self-consistent radiative MHD, given that not only waves but also many other physical processes change the electric fields. To obtain a broader view, we show in Figure 6, in addition to $\delta_s E$, the Alfvén wave power (by computing the velocity projections onto three characteristic directions, e.g., Khomenko & Cally 2011) as follows:

$$v_a = \nabla \times (u_\perp), \tag{10}$$

where $u_\perp$ is the perpendicular component of the velocity to the magnetic field; $|\boldsymbol{J}|/|\boldsymbol{B}|$, which reveals regions with strong tension or reconnection; the Poynting flux; the Lorentz force; and the advective part of the electric field $|\boldsymbol{u} \times \boldsymbol{B}|$. One can appreciate that there is not a single physical process that correlates or connects directly with $\delta_s E$ or Alfvén waves. Some locations with high $\delta_s E$ are associated with several other physical processes. Still, regions with spicules show either the largest values of $|\boldsymbol{J}|/|\boldsymbol{B}|$ or Lorentz force (x = 20, 35 or 40 Mm) as well as $\delta_s E$. In addition to this, those regions generate the strongest Alfvén wave power that penetrates the corona. We find that regions with large $|\boldsymbol{J}|/|\boldsymbol{B}|$ are associated

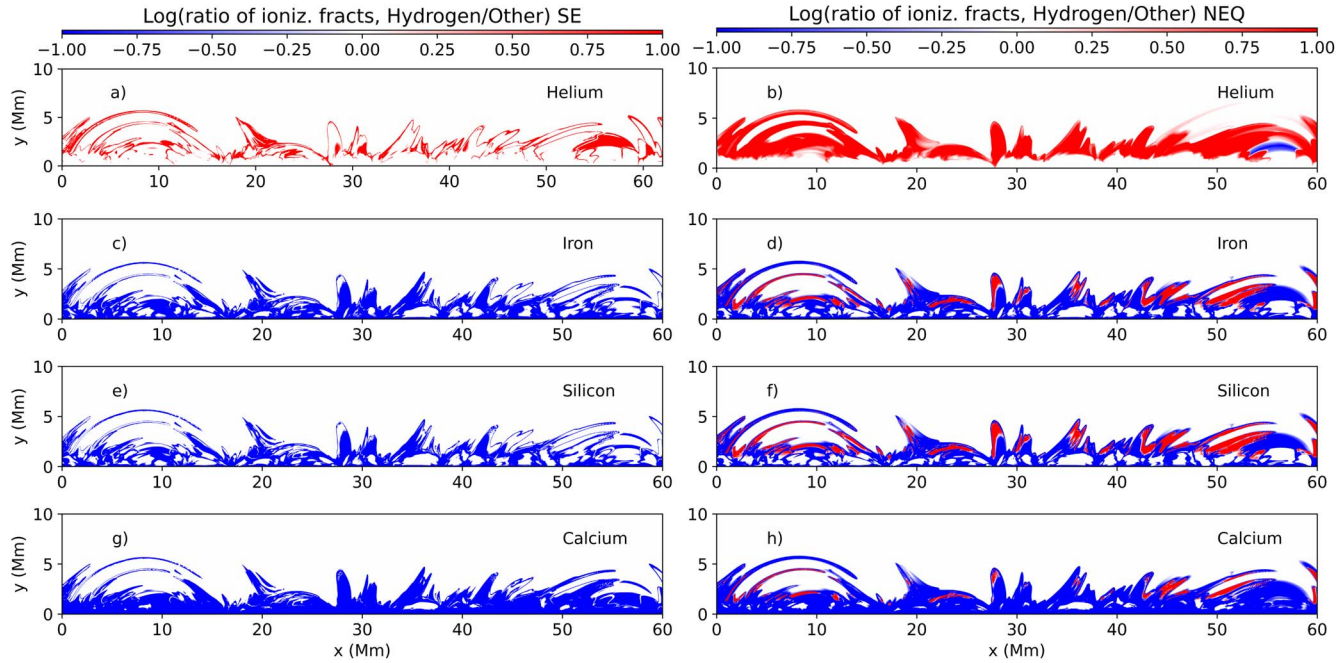

Figure 3. The ratio of the ionization fraction of hydrogen with other species (helium, iron, silicon, and calcium, from top to bottom) reveals where the relative chemical fractionation may happen. Red means hydrogen is ionized whereas the other is neutral, and vice versa for blue. The left column is in SE and the right column NEQ, for hydrogen and helium.

with spicules or low-lying loops interacting with small- and large-scale fields. The field lines connected to large $|\boldsymbol{J}|/|\boldsymbol{B}|$, and hence to large $\delta_s E$ in the chromosphere, show large Alfvén wave amplitude in the transition region and corona. We note that these regions are connected to regions with enhanced magnetic field networks or plage regions. These then are the regions that seem to harbor conditions that are favorable for the ponderomotive force to act. Observationally, these are often regions that show enhanced nonthermal line broadening, as we show in Section 3.2. In principle, high-frequency Alfvén waves can produce large nonthermal velocities of transition region lines. This is because these waves are often unresolved at the temporal and spatial resolution of current instruments (see Section 3.2).

In Section 5.3, we aim to investigate the chromospheric multifluid effects on Alfvén waves using the multifluid and multispecies (MFMS) numerical code Ebysus. In order to initialize our MFMS simulations, we compute within the regions of interest (the nonmasked regions in Figure 5) the populations of each species (four left panels of Figure 7), magnetic field (panels (c) and (g)), and temperature (panels (d) and (h)). The top row is under SE conditions, and the bottom row is for NEQ. Panels (a), (c), (d), (e), (g), and (h) are within the regions of interest for each species, and panels (b) and (f) are for the region of interest of H-Ca (panels (g) and (h) in Figure 5). It should be noted that the regions of interest are where chemical fractionation may happen, because it is relatively weakly collisional and the ionization degree differs between high- and low-FIP elements. To inspire the initial conditions of our MFMS simulations (see below), we use the region of interest of H-Ca, because it covers the largest region where chemical fractionation may happen. From the models, it appears that the field strength ranges from ∼10 G to ∼120 G and the median is around 30 G in those regions where chemical fractionation may occur. For the temperature, there is a clear difference between SE and NEQ scenarios: the former has a narrower temperature range ($\log(T(K)) = [3.4, 4]$) than in NEQ ($\log(T(K)) = [3.2, 4.3]$) and both roughly peak at similar temperatures ($\log(T(K)) \sim 3.7$), but for SE this varies more for each species.

For the following study (Section 5) and to limit the parameter range of the multifluid simulations (which are computationally expensive), we restrict the variation of the magnetic field along the loop and initialize the densities as constant in space (Section 2). This means that we consider 1D loops that expand or constrict with height (and/or direction of wave propagation). One would expect that, on the Sun, the degree of expansion with height of the field would depend on the type of region, e.g., coronal holes, quiet Sun, plage, active regions, etc. We compute the magnetic field strength and Alfvén speed in the region of interest shown in panel (h) of Figure 5 from the 2.5D numerical model, and find that, in our plage simulation, the configuration is much more complex than a simple expansion with height. This would need to be taken into account in the future (Figure 8). For now, inspired by the model field topology, we will parameterize the expansion of the magnetic field as listed in Table 2. The complex magnetic field expansion or canopies have a variation of the magnetic field of roughly $\Delta B \sim \pm 20$ G.

5. Multifluid and Multispecies Simulations of the Ponderomotive Force

In this second part of this manuscript, we introduce the MFMS numerical code Ebysus, including a short description of the physics included and the numerical scheme (Section 5.1). As a continuation, we describe the setup of the parametric study of the various numerical models (Section 5.2), and finally, the results of the MFMS models (Section 5.3).

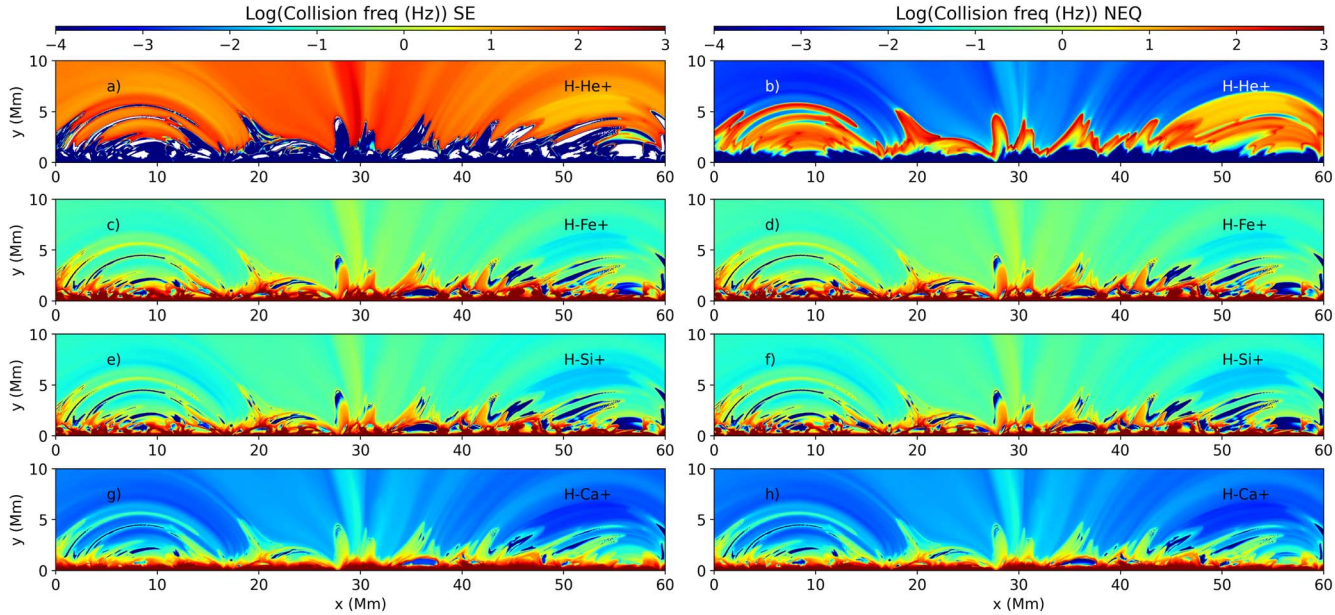

Figure 4. Collision frequency between the neutral hydrogen and the other ionized species (helium, iron, silicon, and calcium, from top to bottom) maps are shown in SE (left column) and NEQ ionization (right column).

5.1. The MFMS Numerical Ebysus Code

The Ebysus code is the first of its kind to treat each excited/ionized level for each desired species as a separate fluid. For this research, although the code includes the following terms, we neglect ionization and recombination, gravity, and the heating or cooling sources from radiation, ohmic diffusion, and thermal conduction. These assumptions allow us to "isolate" and limit the parameter range of the considered dependencies of the ponderomotive force on Alfvén waves. Therefore, the resulting multifluid equations in SI are as follows:

$$\frac{\partial \rho_{\rm aIE}}{\partial t} + \nabla \cdot (\rho_{\rm aIE}\, \boldsymbol{u}_{\rm aIE}) = 0, \tag{11}$$

$$\begin{aligned}\frac{\partial(\rho_{\rm a\hat{I}E}\boldsymbol{u}_{\rm a\hat{I}E})}{\partial t} &+ \nabla \cdot (\rho_{\rm a\hat{I}E}\boldsymbol{u}_{\rm a\hat{I}E} \otimes \boldsymbol{u}_{\rm a\hat{I}E} - \hat{\tau}_{\rm a\hat{I}E} + P_{\rm a\hat{I}E}\mathbb{I}) \\ =&\rho_{\rm a\hat{I}E}\boldsymbol{g} + n_{\rm a\hat{I}E} q_{\rm a\hat{I}}(\boldsymbol{E} + \boldsymbol{u}_{\rm a\hat{I}E} \times \boldsymbol{B}) \\ &+ \sum_{\rm a'I'E'} \boldsymbol{R}_{\rm a\hat{I}E}^{\rm a\hat{I}Ea'I'E'},\end{aligned} \tag{12}$$

$$\begin{aligned}\frac{\partial(\rho_{\rm a0E}\boldsymbol{u}_{\rm a0E})}{\partial t} &+ \nabla \cdot (\rho \boldsymbol{u}_{\rm a0E} \otimes \boldsymbol{u}_{\rm a0E} - \hat{\tau}_{\rm a0E} + P_{\rm a0E}\mathbb{I}) \\ =&\rho_{\rm a0E}\boldsymbol{g} + \sum_{\rm a'I'E'} \boldsymbol{R}_{\rm a0E}^{\rm a0Ea'I'E'},\end{aligned} \tag{13}$$

$$\frac{\partial e_{\rm aIE}}{\partial t} + \nabla \cdot (e_{\rm aIE}\boldsymbol{u}_{\rm aIE}) + P_{\rm aIE}\nabla \cdot \boldsymbol{u}_{\rm aIE} = Q_{\rm aIE}^{\rm visc}, \tag{14}$$

and

$$\frac{\partial e_e}{\partial t} + \nabla \cdot (e_e \boldsymbol{u}_e) + P_e \nabla \cdot \boldsymbol{u}_e = Q_e^{\rm visc}, \tag{15}$$

where the ionization states are referred as "I," i.e., I = 0 denotes neutrals and $\hat{\rm I} = {\rm I} \geqslant 1$ ions. The excited levels are marked with "E," and the identity of the chemical species (or molecules) is indicated by "a." Consequently, each set of particles in a given microstate will be described with "aIE." For electrons, the notation aIE is reduced to just "e." For simplicity, $\sum_{\rm a'}$ is the sum over all the species a′, $\sum_{\rm I',a}$ is the sum over all ionization levels, including neutrals, for a given species a, and $\sum_{\rm E',aI}$ is the sum over all the excited levels for a given ionized species aI. For clarity, we define $\sum_{\rm a'I'E'} = \sum_{\rm a'}\sum_{\rm I',a'}\sum_{\rm E',a'I'}$, and $\sum_{\rm I'E',a} = \sum_{\rm I',a}\sum_{\rm E',aI'}$. The mass density is $\rho_{\rm aIE} = m_{\rm aIE}\, n_{\rm aIE}$, where $\boldsymbol{u}_{\rm aIE}$, $n_{\rm aIE}$, and $m_{\rm aIE}$ are the velocity, number density, and particle mass for a given microstate. Here, $q_{\rm aIE}$, $P_{\rm aIE}$, and $\tau_{\rm a\hat{I}E}$ are the ion charge, gas pressure, and viscous tensor for a specific species. $\boldsymbol{E}$, and $\boldsymbol{B}$ are electric and magnetic field, respectively. $\boldsymbol{R}_{\rm aIE}^{\rm aIEa'I'E'}$ is the momentum exchange, where aIE ≠ a′I′E′. For the collision integrals, we consider neutral–neutral, ion–neutral including charge exchange, or Maxwell molecular collisions, as well as Coulomb collisions between ions following Bruno et al. (2010) (see Wargnier et al. 2022, for further details on the collisions and cross-sections). The momentum exchange can then be expressed as follows:

$$\boldsymbol{R}_{\rm aIE}^{\rm aIEa'I'E'} = m_{\rm aIE}\, n_\alpha\, \nu_{\rm aIEa'I'E'}(\boldsymbol{u}_{\rm a'I'E'} - \boldsymbol{u}_{\rm aIEa}), \tag{16}$$

where $\nu_{\rm aIEa'I'E'}$ is the collision frequency. We note that, to guarantee the conservation of the total momentum, $\boldsymbol{R}_{\rm aIE}^{\rm aIEa'I'E'} = -\boldsymbol{R}_{\rm a'I'E'}^{\rm a'I'E'aIE}$. $Q^{\rm visc}$ is the viscous heating due to hyperdiffusion.

We ignore electron inertia and its time variation. So, in Ebysus, we consider the magnetic induction equation:

$$\begin{aligned}\frac{\partial \boldsymbol{B}}{\partial t} &= -\nabla \times \boldsymbol{E} \\ &= \nabla \times \left(\boldsymbol{u}_e \times \boldsymbol{B} - \frac{\nabla P_e}{n_{\rm e} q_{\rm e}} + \frac{\sum_{\rm aIE} \boldsymbol{R}_{\rm e}^{\rm eaIE}}{n_{\rm e} q_{\rm e}} \right).\end{aligned} \tag{17}$$

The second and third terms here are the Bierman battery and the ohmic diffusion, respectively, and we ignored the ionization recombination contribution to the electric field. Because electrons move so fast and their mass is negligible, we assume

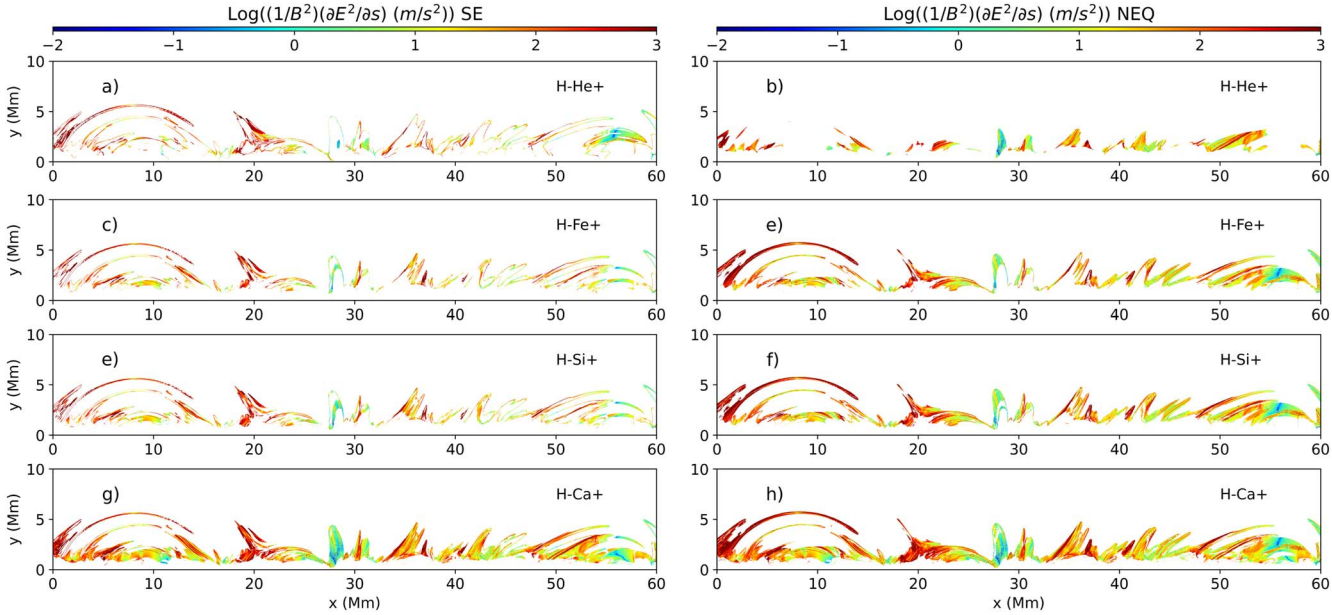

Figure 5. Maps of the electric field variations along the loop (Equation (9)). In these maps, we have masked out regions with high collision rates (>10 Hz) for each element (Figure 4), as well as regions where they have the same ionization state as hydrogen (Figure 3). The region of interest (nonmasked region) is where the ponderomotive force may produce chemical fractionation. The distribution of the various panels is the same as in Figure 4.

quasi-neutrality: $n_e = \sum_{aIE} n_{aIE} Z_{aI}$, where Z_{aI} is the ionized state, and we neglect their inertia. Because several ionized species are considered, the electron velocity, thanks to the assumption of quasi-neutrality, reads as follows:

$$\boldsymbol{u}_e = \left(\sum_{a\hat{I}E} \frac{n_{a\hat{I}E} q_{a\hat{I}E} \boldsymbol{u}_{a\hat{I}E}}{n_e q_e} \right) - \frac{\boldsymbol{J}}{q_e n_e}, \tag{18}$$

and $\boldsymbol{J} = (\nabla \times \boldsymbol{B})/\mu_0$. We refer to the total ion velocity as $\boldsymbol{u}_c = \sum_{a\hat{I}E} \boldsymbol{u}_{aIE}$, and that for neutrals as $\boldsymbol{u}_n = \sum_{a0E} \boldsymbol{u}_{a0E}$.

Ebysus has inherited the numerical methods from Bifrost (Gudiksen et al. 2011), and the first results of this code can be found in Martínez-Sykora et al. (2020). In short, the numerical mesh is defined in a staggered Cartesian box. The spatial derivatives and interpolation of the variables are sixth- and fifth-order polynomials, respectively. To advance in time, we selected to advance explicitly, by stepping forward in time using the modified explicit third-order predictor-corrector Hyman method (Hyman 1979). Finally, the numerical noise is suppressed using a high-order artificial diffusion. Further details on Ebysus will be described in a dedicated manuscript for the code.

5.2. Initial and Boundary Conditions

We investigate the effects of MFMS interactions and SE versus NEQ ionization on the ponderomotive force due to Alfvén waves in a parametric study for chromospheric conditions. The density and temperature are taken from the median of the histograms in Figure 7, assuming the region of interest from panels (d) (SE) or (h) (NEQ) in Figure 5 and listed in Table 1. We consider one SE case. For computational reasons, we had to select higher ion densities in order to be able to run this SE scenario for hydrogen and helium. This is because the very different range of values of number density for the various fluids leads to computational complications. The temperature is constant with 1.6×10^4 K. Finally, the magnetic field follows a quarter of a sinusoidal profile that varies within the values listed in the sixth column of Table 2, where the first number is at the bottom and the last is at the top. It should be noted that the divergence of the magnetic field is not zero in 1.5D. Therefore, in principle, by adding dimensions or assuming that the loop "width" changes with height, the divergence will be zero. For the purpose of those experiments, we consider that the magnetic field is expanding and this background configuration does not change in time. In addition, the divergence of the magnetic field is small compared to the Aflven wave variation. The range for the Alfvén speed is listed in the sixth column. The values and range of the magnetic field and Alfvén speed are similar to the parameter range within the region of interest shown in Figure 8, except near the transition region, where the Alfvén speed variations with height can become much larger than the range covered here. Because we assume constant densities, the variation of the Alfvén speed in the box has the sign opposite to that of the magnetic field. This is contrary to what would be expected on the Sun, because the density stratification leads to an increase in Alfvén speed with height, despite the decrease in magnetic field strength expected from an expanding flux tube. This should be considered when we refer to the magnetic field variation along the loop as the "expansion" or "constriction" of field lines in loops. The variation of the Alfvén speed along the loop is expected to play a significant role in ponderomotive force and is thus not fully considered here, given our constant-density assumption.

The numerical domain in all 1.5D numerical experiments is along the loop, which for the MFMS models will be the z-axis, and covers the range $z = [0, 3]$ Mm with a uniform grid of 1000 points, which is roughly the length where the fractionation may occur in panel (j)) of Figure 5. The grid spacing has been chosen to resolve spatially and temporally the Alfvén waves for any simulation. It should be noted that $z = 0$ is not the photosphere as in the previous section, but the range $z = [0, 3]$ Mm covers a subregion within the chromosphere. In all of our simulations, waves are launched from $z = 0$ Mm and propagate toward positive values of z. As the wave propagates, it will

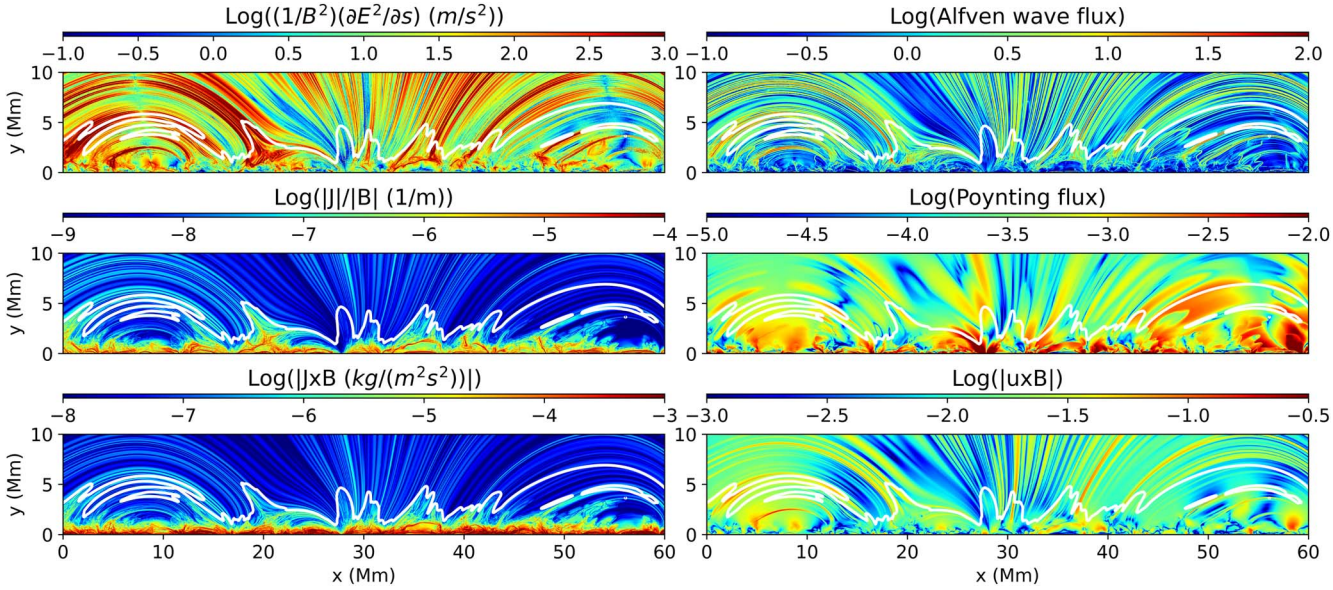

Figure 6. Various physical processes play a different role in different features. $\delta_s E$ following Equation (9), the Alfvén wave power, $|J|/|B|$, Poynting flux, Lorentz force, and advection term of the electric field are shown from left to right and top to bottom, respectively. The solid line is at temperature 10^5 K.

either encounter an increase of magnetic field strength (i.e., a constricting flux tube) or a decrease of magnetic field strength (i.e., an expanding flux tube).

The boundaries are open at the "top" of the domain. At the "bottom," we drive an Alfvén wave along the component x of the magnetic field with different frequencies and amplitudes listed in the two rightmost columns of Table 2. We put quotation marks around the words "top" and "bottom" because our numerical experiments do not include gravity. The bottom to top direction is really the direction of wave propagation. We note that the frequencies are inspired by the observational constraints in Section 3, and the selected amplitudes are a fraction of the velocity amplitudes derived from the nonthermal velocity, assuming that not all of the broadening is caused by Alfvén waves. Another reason to not use large amplitudes is to avoid nonlinear effects in this initial study. Columns 2–5 list which physical processes are included in each of the simulations.

5.3. Results of the MFMS Models

In Section 2, we emphasized the challenging work of selecting the proper assumptions needed in order to choose the appropriate ponderomotive force. In contrast, the Ebysus code self-consistently solves the multifluid equations for various species without considering any of those particular assumptions. As we will show, the assumptions required for calculating the ponderomotive forces can be very limiting, which can lead to an overestimation or misjudgement of their impact on the plasma dynamics.

The ponderomotive force depends on the variation of the electric field along the loop, while the electric field associated with Alfvén waves depends on the wave energy. Therefore, first, we investigate the velocity and magnetic field variation as a function of space. This will help to understand the variation of the electric field with the distance along the loop (i.e., magnetic field lines). These gradients are ultimately responsible for the acceleration along the loop.

Let us focus first on a case without collisions, e.g., NC_B7050_F1_D1. Figure 9 shows various physical parameters as a function of space once the wave has propagated through most of the domain. Because there are no collisions, neutral fluids do not experience any variation in space and time as a result of an Alfvén wave. However, it is interesting to see a rotation of the ion velocities (second row) and magnetic field (bottom row, in red) perpendicular to the guided field, as shown with the two perpendicular components (x and y in the first and second columns). The rotation is due to the ion coupling between the various ionized fluids as reported by Martínez-Sykora et al. (2020) and not because of the Hall term. The equivalent simulation without the Hall term (NH_B7050_F1_D1) also has this rotation (not shown here). The ion coupling leads to a velocity drift between different ions (fourth row). Furthermore, due to the expansion of the magnetic field, i.e., a magnetic field strength decrease with z and similarly with the Alfvén speed, there is an upflow in the ion velocity (right column), which can produce a chemical fractionation depending on the ionization fraction of each species. It is also interesting to see the amplitude of the ion velocities (panels (e)–(h)) and the perpendicular component of magnetic field (panels (q)–(s)) increase. The wavelength decreases with z, i.e., with the decrease of the magnetic field (panel (t), red), This is expected from a propagating Alfvén wave in a medium where the Alfvén speed decreases with z. We note that the Alfvén speed follows the magnetic field strength because the density and temperature are constant.

This picture changes drastically when collisions are included, e.g., A_B7050_F1_D1 (Figure 10). Neutrals are being dragged by the ions (top row), and the velocity patterns for each neutral fluid are shifted spatially because of a phase shift, which depends on the collision frequency with other ions. Still, neutrals are not completely coupled with ions, and a small velocity drift is present (third row). As a result, the wave power, i.e., the velocity perpendicular to the magnetic field, drops while it propagates along the z-axis, i.e., dissipation occurs. Interestingly, vertical flows are much larger than the collisionless scenario shown above. As with the amplitudes, the vertical velocities drop drastically with z, in contrast to the previous case. This is because of the presence of collisions.

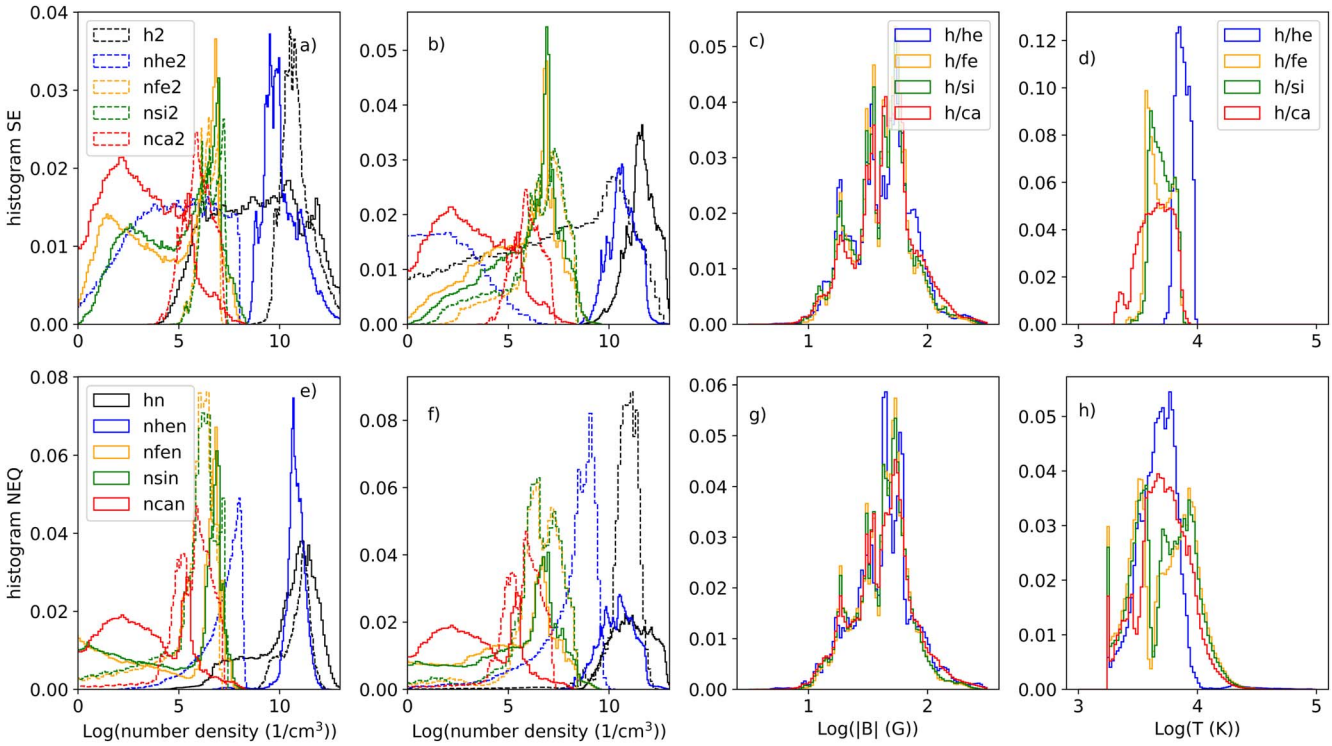

Figure 7. Histogram of the density population for neutrals (solid; panels (a), (b), (e), and (f)) and ions (dashed; panels (a), (b), (e), and (f)), magnetic field (third column) and temperature (right column) within the regions of interest (nonmasked regions) in Figure 5, for each species (panels (a), (c), (d), (e), (g), and (h)). Panels (b) and (f) are for the region of interest of H-Ca. SE case is in the top row and NEQ in the bottom row.

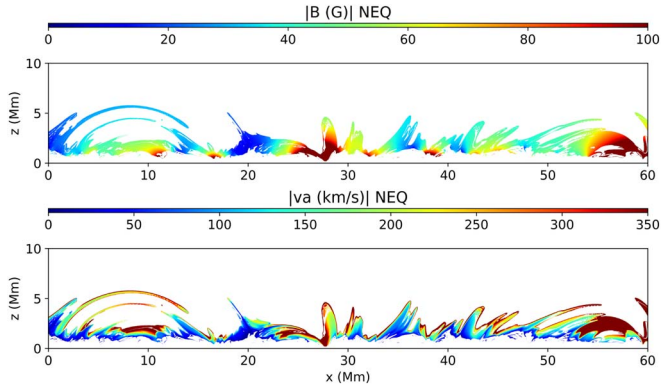

Figure 8. Magnetic field strength (top) and Alfvén speed (bottom) maps, where we applied the same mask as in panel (h) in Figure 5, revealing the complexity of the expansion or canopies of the magnetic field topology within the regions of interest.

Table 1
Density Number of the Various Fluids

Species	Neutrals (NEQ, SE)	Ions (NEQ, SE)
H	$10^{9.8}$, $10^{11.1}$	$10^{10.7}$, $10^{8.5}$
He	$10^{9.7}$, $10^{10.6}$	$10^{8.3}$, $10^{4.8}$
Fe	$10^{4.6}$, $10^{5.25}$	$10^{5.6}$, $10^{6.4}$
Si	$10^{4.7}$, $10^{5.7}$	$10^{5.4}$, $10^{6.2}$
Ca	$10^{2.7}$, $10^{2.5}$	$10^{5.3}$, $10^{5.9}$

Note. From left to right: the species and the number density for the neutral and ionized fluid in cm^{-3}.

Neutrals show relatively large velocity drifts, which result from a vertical velocity variation with z due to collisional coupling, which does not occur in the collisionless scenario shown previously. Consequently, the multifluid interactions lead to a mix of wave phases between the various fluids, producing dissipation and a large contribution to the ponderomotive force (as shown below) compared to the collisionless case shown above.

We now study the role of the parameters listed in Table 2 on the variation of the wave properties as a function of z (i.e., the direction of wave propagation, not necessarily height). To this end, we calculate (and show in Figure 11) the gradient with z of the peaks of the oscillations for the various types of velocities: perpendicular to the field (first and third rows, for neutrals and ions, respectively), along the field (second and fourth rows, for neutrals and ions, respectively), and the total velocity of all fluids combined (fifth row). As we can see, most of the cases we studied show a negative gradient with z, i.e., a decrease with increasing z, except for a few cases without collisions. An increase in the amplitude (first column) or frequency (second column) of the driver leads to stronger gradients of velocities with z and greater drifts for neutrals (top panels) in both perpendicular and longitudinal motions. The slopes of the various variables as a function of the background magnetic field variation with z provide a fascinating result. For all the collisional cases, the slopes are negative, regardless of whether the loop is expanding ($\Delta B < 0$) or constricting ($\Delta B > 0$) in the direction of wave propagation. The slopes of the collisionless cases (shown with dots) clearly have different signs (panels (m) and (n)), i.e., the sign is positive for $\Delta B < 0$ (expanding) and negative for $\Delta B > 0$ (constricting). For the collisional cases, the gradient with z for all variables increases with increasing magnetic field expansion (decreasing ΔB for all negative ΔB

Table 2
List of Numerical Simulations

Name	Ohm	Coll	Hall	B Range (G)	v_A (km s^{-1})	Fr. (Hz)	B Amp. Wave (G)
NH_B7050_F1_D1	No	No	No	[70, 50]	[290, 210]	1	0.1
NC_B7050_F1_D1	No	No	Yes	[70, 50]	[290, 210]	1	0.1
NC_B5070_F1_D1	No	No	Yes	[50, 70]	[210, 290]	1	0.1
C_B7050_F1_D1	No	Yes	Yes	[70, 50]	[290, 210]	1	0.1
C_B5070_F1_D1	No	Yes	Yes	[50, 70]	[210, 290]	1	0.1
A_B8040_F1_D1	Yes	Yes	Yes	[80, 40]	[330, 170]	1	0.1
A_B6555_F1_D1	Yes	Yes	Yes	[60, 55]	[270, 220]	1	0.1
A_B5070_F1_D1	Yes	Yes	Yes	[50, 70]	[210, 290]	1	0.1
A_B7050_F10_D1	Yes	Yes	Yes	[70, 50]	[290, 210]	10	0.1
A_B7050_F2_D1	Yes	Yes	Yes	[70, 50]	[290, 210]	2	0.1
A_B7050_F01_D1	Yes	Yes	Yes	[70, 50]	[290, 210]	0.2	0.1
A_B7050_F1_D5	Yes	Yes	Yes	[70, 50]	[290, 210]	1	0.5
A_B7050_F1_D1	Yes	Yes	Yes	[70, 50]	[290, 210]	1	0.1
A_B7050_F1_D05	Yes	Yes	Yes	[70, 50]	[290, 210]	1	0.05
A_B7050_F1_D01	Yes	Yes	Yes	[70, 50]	[290, 210]	1	0.01
SE_B5070_F1_D1	Yes	Yes	Yes	[70, 50]	[225, 160]	1	0.1

Notes. From left to right: the name, whether physical processes are included or not, magnetic field configuration, Alfvén speed range, and frequency and amplitude of the Alfvén wave driver. In the fifth column, the first value of the B range is the bottom boundary, and the second is the top, so [70, 50] G is a loop, such that its magnetic field strength decreases with z, i.e., the direction of wave propagation.

cases). We will go into further details below. Finally, one can appreciate that the important physical processes are the presence of collisions, and in more minor roles, the ohmic diffusion and the Hall term (right column). Ncoll refers to simulation NC_B5070_F1_D1 (solid lines) and NC_B7050_F1_D1 (dots without lines), i.e., they do not include collisions nor ohmic diffusion. Nhall refers to NH_B7050_F1_D1, i.e., without collisions, without ohmic diffusion, and without the Hall term. Finally, Nohm refers to C_B7050_F1_D1, i.e., without ohmic diffusion. In the right column, we added the impact of the SE initial setup. Due to the differences in the populations of the various species, the interactions between species and the gradients of the electric field, and hence the ponderomotive force, change dramatically compared to the NEQ case. In SE, the neutral density is higher than the ion density, which results in a stronger dissipation of the Alfvén wave and coupling between ion and neutral fluids. Here again, we added dots for the noncollisional cases for different magnetic field configurations, for comparison.

In order to study the variation of the acceleration for different fluids as a function of the physical parameters, first, we visualize the same variables as in Figure 10 (which are as a function of space for a given time), but now as a function of time at $z = 0.18$ Mm. We note that there is no variation in the wave amplitude with time (Figure 12). Therefore, the electric field has no dependence on time. Consequently, the second term in the parenthesis of Equation (1) is expected to be negligible. Neutral fluids, as mentioned above, experience a different phase speed, due to the differences in collisional frequencies. We also note that neutral fluids experience more significant differences in vertical velocities than ions, because the latter are magnetized and move with the magnetic field. A similar effect can be seen for the gradients with z, as shown in Figure 10. Again, one can appreciate that there is a large phase mixing between the different types of fluids, which leads to the ponderomotive force, as we show below.

We now calculate in Figure 13 the gradients with time of the local maximum velocities in the z direction (right column) of neutrals (top) and ions (bottom) shown with red dashed lines, similarly as for Figure 11, but in time. This figure shows the estimates of the acceleration (in the direction of wave propagation) of the various fluids. The comparison of these accelerations, for each physical process, initial plasma properties, or imposed driver, allows us to further understand the action of the ponderomotive force associated with Alfvén waves in the chromosphere for various fluids (Figure 13). The acceleration increases with the amplitude and frequency of the driver. We remind the reader that the selected frequencies are inspired by IRIS observations (Section 3). It is very intriguing that the acceleration increases with frequency, whereas Equations (1)–(3) are proportional to $1/\omega^2$. As shown in the third column, in the presence of collisions, there is always an acceleration in the direction of the wave propagation, no matter whether the flux tube is expanding or constricting. There is some decrease in the acceleration with an increase in the expansion of the magnetic field, i.e., values of decreasing ΔB for the cases where ΔB is negative. If we assume that a loop expands with height, and also assume a collisional case, the plasma is accelerated in the same direction as the propagating waves. However, in the collisionless cases, if the loop constricts ($\Delta B > 0$), plasma is accelerated in the direction of wave propagation, while if the loop expands ($\Delta B < 0$), plasma

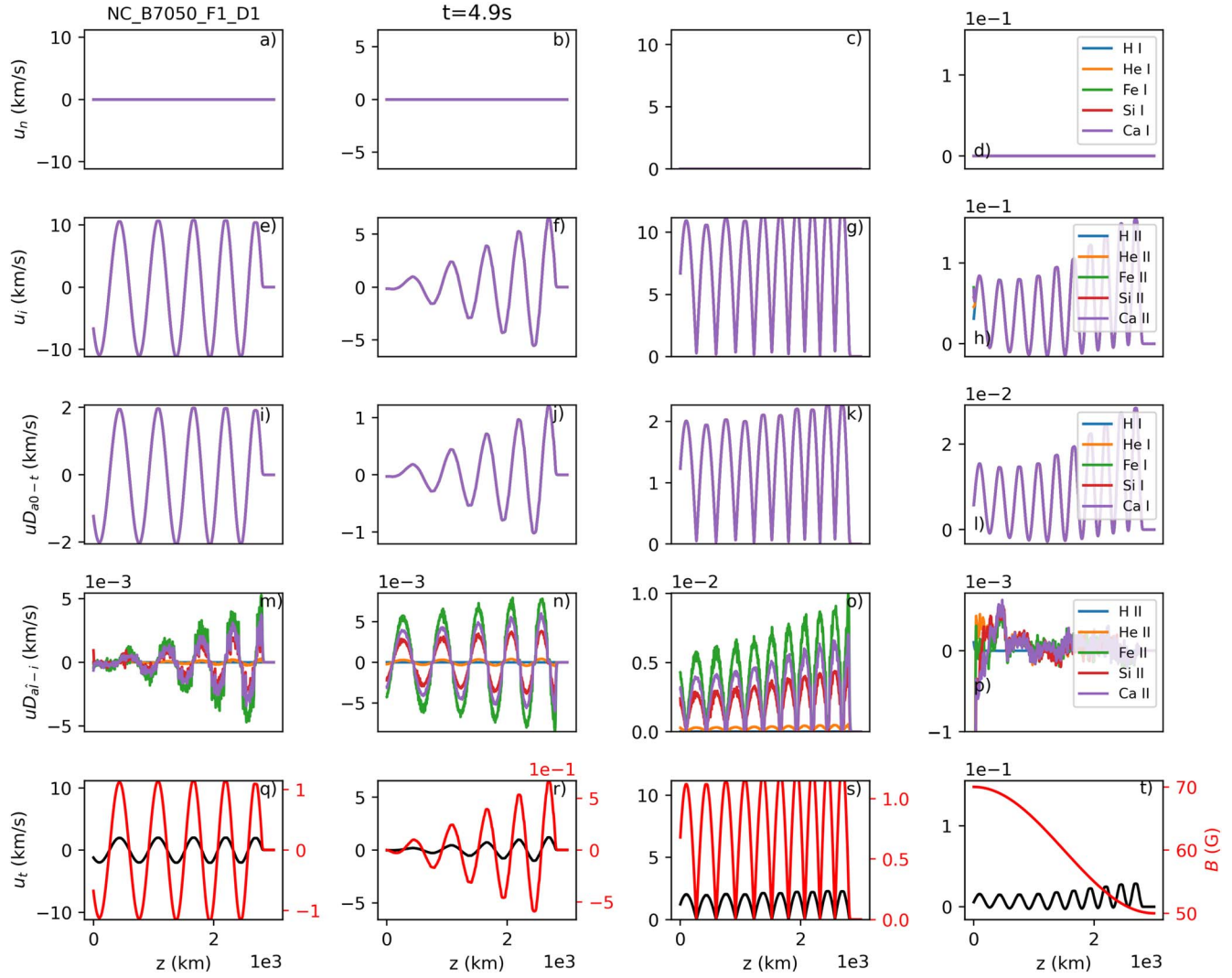

Figure 9. Spatial variation at t = 5 s of velocity for all the neutral species (top row) and ion species (second row), velocity drift for each neutral fluid with respect to the total velocity of all fluids (third row), and velocity drift for individual ion-fluids with respect to the combined fluid of ions (fourth row). In the bottom row, we show the magnetic field (red) and single-fluid velocity, i.e., the total velocity of all fluids (black). For all rows, we show the x component, the y component, the absolute value of the component perpendicular to the guide field, and the z component, from left to right columns, respectively. This figure is for simulation NC_B7050_F1_D1, i.e., it excludes collisions. In this case, the field strength decreases in the direction of wave propagation (e.g., for a wave propagating upward in a loop that expands with height).

is accelerated in the direction opposite that of the wave propagation. If we assume that a loop expands with height, and assume also no collisions, this would mean that plasma is accelerated downward for upward-propagating waves, and downward for downward-propagating waves. It appears that, for the collisionless case, the sign disagrees with Equations (2)–(3), but agrees with the sign of Equation (1). In any case, the presence of collisions leads to a major qualitative and quantitative difference.

Finally, the large accelerations result from collisions that lead to a vital phase mixing between the fluids, as shown in the right column in Figure 13. We also note the large difference between the SE and NEQ cases. In SE, the number density of neutrals is very large and collisions are high. Consequently, waves are damped within a very short traveled distance, and the upflows and acceleration are highly localized closer to the source of the wave ($z \sim 0$).

We notice that, for higher wave frequencies or amplitudes, collisions dissipate the wave faster. Therefore, the accelerations in those cases are highly localized closer to the driver. Further away from the driver (which is at $z = 0$), the spatial gradients of the variables and acceleration are close to zero. This is similar, as mentioned above, to the SE case. In the latter case, this due to the strong coupling with neutrals.

In order to understand the cause of the vertical acceleration as a function of the various parameters, we compute (and show in Figure 14), as a function of z, the electric field perpendicular to the magnetic field (top row), $-dE_\perp^2/dz$ (again calculated based on peaks associated with the wave) as it quantifies the ponderomotive acceleration (middle row), and the Alfvén speed (bottom row). In our simulations, we find a negligible value for dE^2/dt, so we only consider the spatial gradient for E^2 in our proxy for the ponderomotive force. The dependence of the acceleration on the parameters shown in Figure 13 can be understood by investigating the panel that shows $-dE_\perp^2/dz$ in the middle row of Figure 14:

1. The greater the amplitude of the Alfvén wave (panels (a) and (e) in Figure 13), the larger the values in the

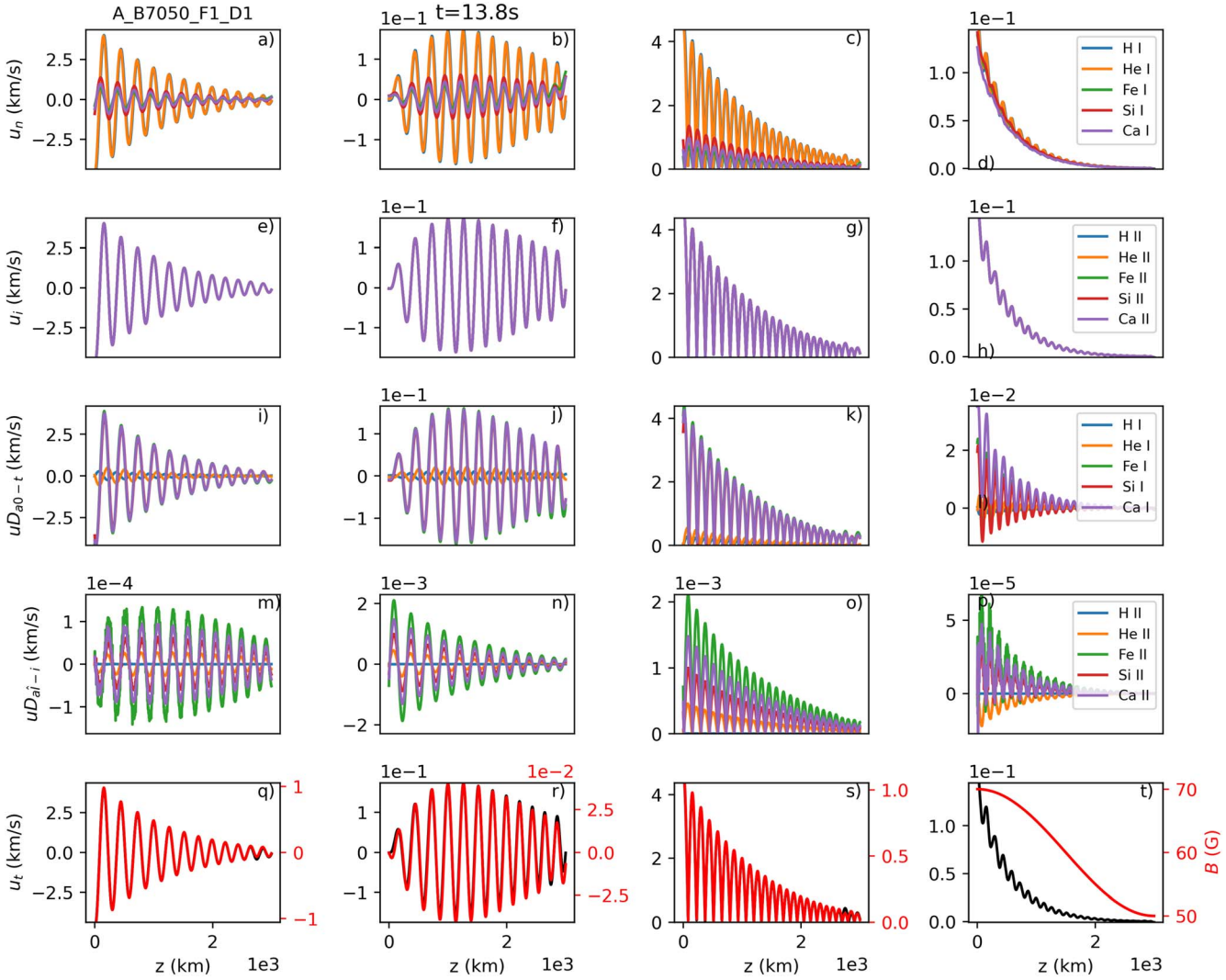

Figure 10. Same layout as Figure 9 for simulation A_B7050_F1_D1, i.e., with collisions and for a decreasing field strength in the direction of the wave propagation (i.e., for a wave propagating upward in a loop that expands with height).

estimated ponderomotive force ($-dE_\perp^2/dz$) (panel (e) of Figure 14).

2. The higher the frequency of the Alfvén wave (panels (b) and (f) in Figure 13), the larger the values in the estimated ponderomotive force (panel (f) of Figure 14). We note that the force drops faster with z, when the frequency is higher. This is because of the strong dissipation.
3. Due to collisions, $E_\perp$ decreases with z for any background field configuration considered here (ΔB). This results in a positive ponderomotive force (i.e., in the direction of wave propagation) for constricting and expanding loops. There is a decrease in the acceleration and ponderomotive force when increasing the expansion of the field lines, i.e., with decreasing ΔB. Still, the presence of collisions has a stronger impact on the ponderomotive force and acceleration than the variation of the field configuration and Alfvén speed (panel (k)).
4. The collisionless cases reveal the large role of collisions. Indeed, for an expanding or constricting loop, the sign of the acceleration changes, being positive for constricting loops ($\Delta B > 0$) and negative for expanding loops ($\Delta B < 0$) (dots in panels (c), (d), (g), and (h) in Figure 13). This is in agreement with the $E_\perp$ dependence with z, i.e., $E_\perp$ decreases in the direction of the propagating wave (with z) for a constricting loop (red and purple lines in panels (d), (h), and (l) in Figure 14) (because the Alfvén speed increases), and as a result, the estimated ponderomotive force is positive. In contrast, for an expanding loop, $E_\perp$ increases in the direction of the propagating wave (brown lines panels (d), (h), and (l) in Figure 14) (because the Alfvén speed decreases), and as a result, the estimated ponderomotive force is negative. We note that the sign of this acceleration follows Equation (1).
5. The initial setup of the density population (NEQ versus SE) greatly impacts the electric field changes with z, and hence the estimated ponderomotive force and acceleration of the various fluids, as shown previously.
6. The motions in the perpendicular plane (and electric field) are very similar between the NC_B7050_F1_D1 case and NH_B7050_F1_D1, i.e., with and without the Hall term.

It is clear that collisions play a critical role in the ponderomotive force within the parameter range considered here (Tables 1 and 2), which is inspired by chromospheric values. This is shown in the right columns in Figures 11, 13,

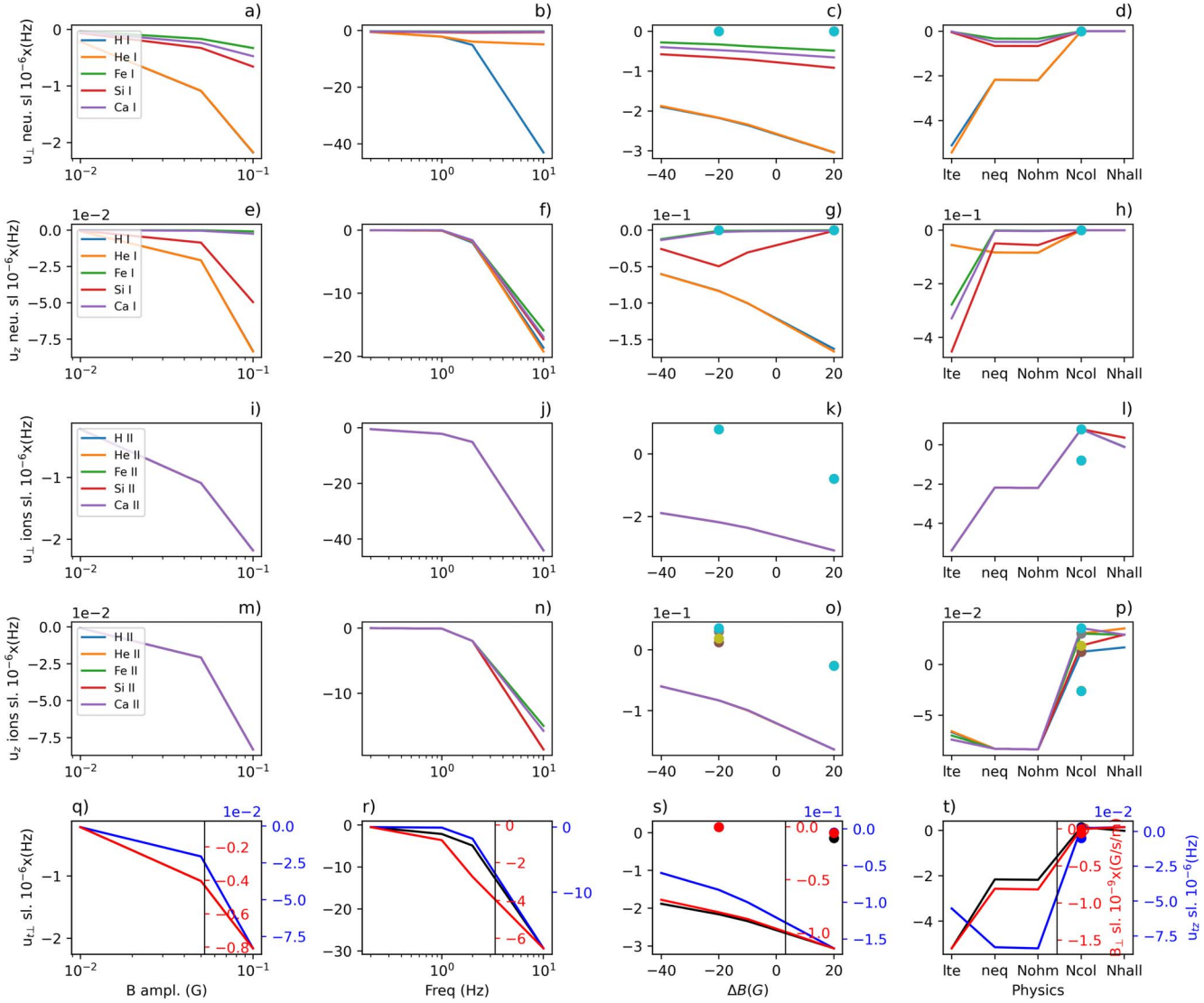

Figure 11. The median of the spatial gradient with z of the wave-associated velocities that are perpendicular to the field (first and third rows) and longitudinal (second and fourth rows) for neutrals (top two rows) and ions (third and fourth rows). We plot these as a function of amplitude and frequency of the Alfvén wave driver, variation of the guide magnetic field, and inclusion of various physical approaches, respectively, from left to right. The last row shows the spatial gradient with z for wave-associated velocities (for all fluids combined) that are perpendicular to the field (black) and longitudinal (blue). We also show, in the bottom row, the spatial variation of the perpendicular component of the magnetic field (red). The collisionless cases have been added with dots in the two right columns.

and 14. The sign of the ponderomotive acceleration agrees with that found in Equation (1). However, as shown in Figure 15, the ratio of the acceleration with ($-dE_\perp^2/dz$) does not follow $1/\omega^2$, but it does follow ω^2. This dependence is, however, in agreement with the predictions from damping of Alfvén waves, as shown for the example from ion–neutral interactions (Haerendel 1992; De Pontieu & Haerendel 1998). For this ion–neutral damping, the predicted damping length L for the wave field is given in Equation (8) and can be compared with the distance over which the wave field $E_\perp^2$ decays in the top row of Figure 14. The damping length in our simulations is shorter than what is predicted from the simplified analytical calculations of Haerendel (1992) and De Pontieu & Haerendel (1998), and it shows a discrepancy of $\sim$6. There are multiple reasons for this mismatch. For example, the theoretical predictions are based on a single-fluid approach that does not properly treat the effects of multiple neutral and ion species. It also assumes a WKB approach, i.e., small changes over a wavelength. Most importantly, in our case, it ignores any interactions between different neutral species, such as hydrogen and helium. As we can see in Figure 10, the neutral helium develops a significant drift with respect to the other neutral species (most importantly hydrogen, which carries most of the mass), which rapidly leads to slippage between these important constituents of the plasma, leading to phase mixing and damping of the Alfvén wave. The latter occurs because the neutrals are very well coupled to the ions and thus impact the electric field associated with the Alfvén wave, leading to dissipation. We note that we expect that wave damping, whether through ion–neutral or neutral–neutral interactions, would both lead to a ponderomotive force that is proportional to $-dE_\perp^2/dz$.

It should be noted that the setup of the simulations allows considering scenarios where the Alfvén wave is driven from "above," i.e., the corona, or "below," i.e., the photosphere. Let us assume a loop that expands with height. Under those highly simplified scenarios, i.e., no density stratification nor reflections, and assuming the collisionless case, a wave coming from the corona will see a loop that constricts (i.e., $\Delta B > 0$) in the

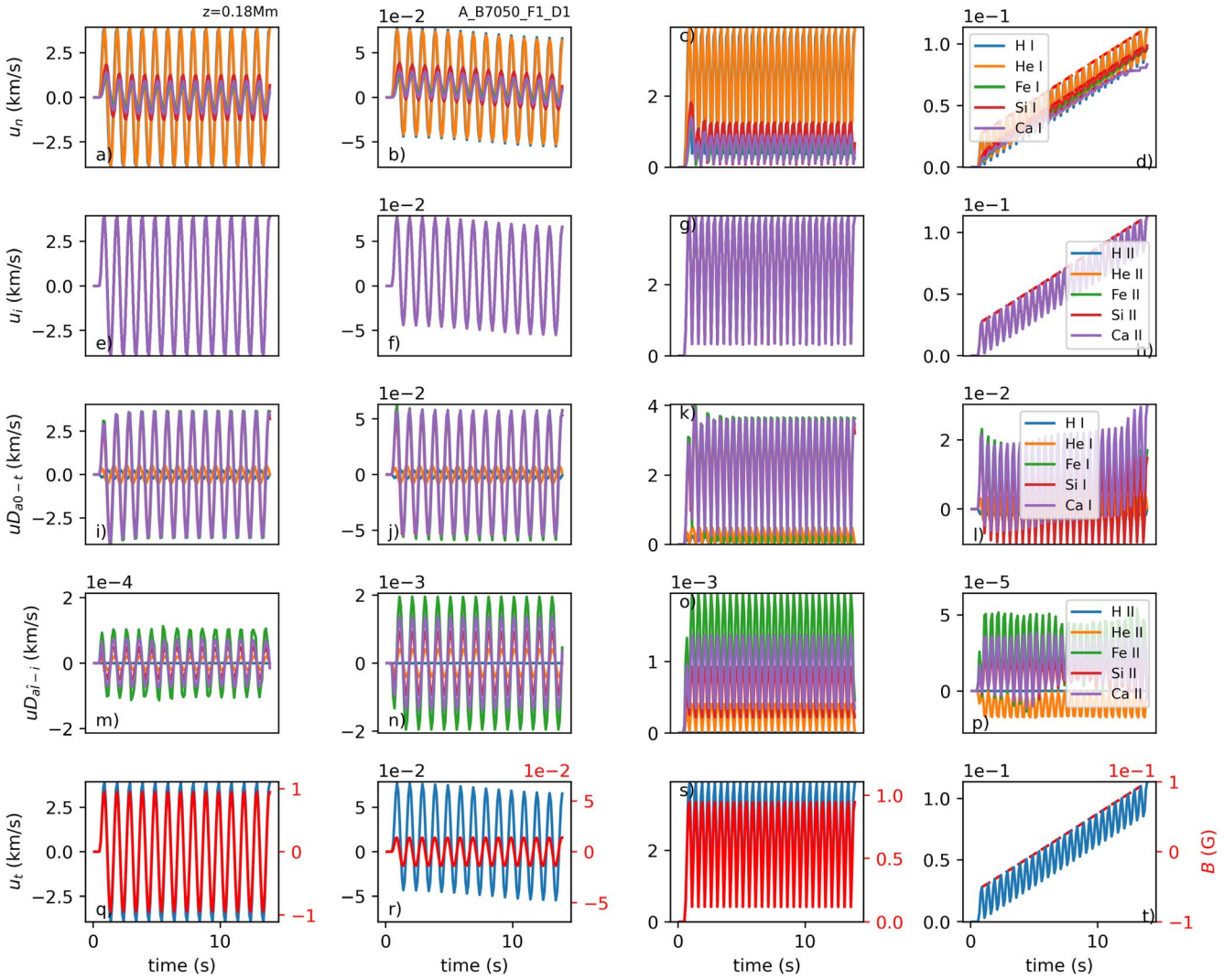

Figure 12. Temporal variation at $z = 0.18$ Mm of velocity for all the neutral species (top row), ion species (second row), velocity drift for each neutral fluid with respect to the total velocity of all fluids (third row), and velocity drift for individual ion-fluids with respect to the combined ion-fluid (fourth row). In the bottom row, we show the magnetic field (red) and single-fluid velocity, i.e., the total velocity of all fluids (black). For all rows, we show the x component, the y component, the absolute value of the component perpendicular to the guide field, and the z component, from left to right columns, respectively. This figure is for simulation A_B7050_F1_D1, i.e., with collisions and a decreasing magnetic field strength with z.

direction of the wave propagation. Our model shows that this will produce an acceleration in the direction of the wave propagation (the right dot in the third column of Figure 13), i.e., downward. This could potentially cause the inverse FIP effect. In contrast, a wave coming from the chromosphere along the same expanding loop will see an expanding loop in the direction of the wave propagation. In the collisionless case, this would lead to a force in the direction opposite to that of the wave propagation, i.e., also downward (the left dot in the third column of Figure 13, $\Delta B < 0$). This would again lead to an inverse FIP effect. However, collisions will lead to a ponderomotive force in the direction of the wave propagation independently of the field configuration, producing acceleration in the direction of the wave propagation. This would imply the FIP effect for a wave coming from below, and could imply an inverse FIP effect for a wave coming from the corona.

6. Discussion and Conclusions

One of the most generally accepted models to explain the FIP effect is based on the effects of the ponderomotive force, using semi-empirical models (e.g., Laming 2004). In this study, by combining IRIS observations with single and multifluid models, we go beyond the limitations of those assumptions. We investigate the possible role of the ponderomotive force on accelerating the plasma by considering multifluid effects and the ionization under SE and NEQ conditions.

Being aware of the complexity of the mixture of waves in the solar atmosphere and LOS effects (De Pontieu et al. 2004; Okamoto & De Pontieu 2011), we used nonthermal velocities from a transition region line, i.e., Si IV from IRIS observations to provide constraints on the properties of unresolved high-frequency waves. Assuming that the nonthermal broadening can be ascribed to waves, one can estimate their lowest frequencies and highest amplitudes. We found that plage and network field regions experience the largest nonthermal velocities.

Using the radiative MHD numerical model described in Martínez-Sykora et al. (2020), we investigate the properties of the regions of interest where low- and high-FIP elements first ionize in the solar atmosphere for a plage region. Our analysis

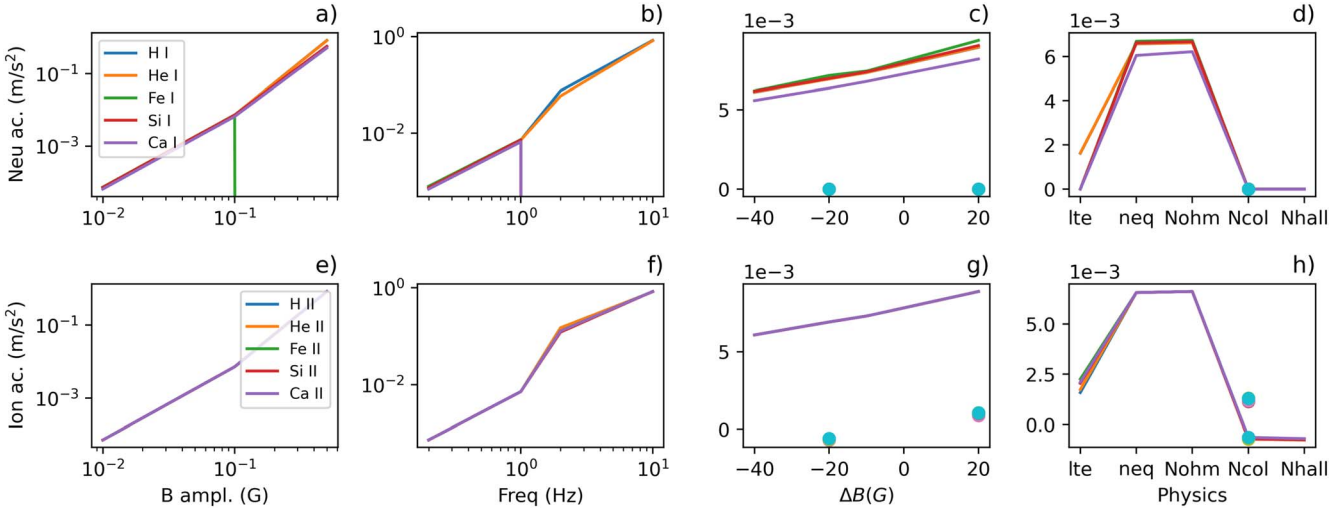

Figure 13. The median of the vertical acceleration at $z = 0.18$ Mm for neutrals (top row) and ions (bottom row) as a function of Alfvén wave amplitude and frequency, the guided magnetic field variation, and physics are shown from left to right.

reveals that, in the chromosphere, the largest perturbations of the electric field component perpendicular to the magnetic field occur in areas of enhanced network field or plage regions, associated with type II spicules and large changes in the magnetic field topology. Chromospheric spicules occur most frequently around the network field that is concentrated at the edges of supergranular cells, i.e., where nonthermal broadening in the low TR is enhanced (see also Pereira et al. 2014). In simulations of spicules, they are associated with strong currents and drive Alfvén waves (Martínez-Sykora et al. 2017), suggesting that, if the ponderomotive force indeed drives the FIP effect, this could lead to chemical fractionation. Our results reveal that the NEQ effects largely impact the region where the chemical fractionation may occur within the chromosphere and needs to be considered when studying the FIP effect. We note that the recent work by Wargnier et al. (2023) provides another possible chemical fractionation mechanism that depends on the history of the multifluid evolution for reconnection events. Brooks et al. (2015) observational studies connect strong outflows and active or plage regions with locations with high FIP bias. It should be noted that our setup is inspired by strong magnetic fields such as plage regions (see Table 2 and Figures 7 and 8).

In the last part of this manuscript, inspired by our observational and single-fluid analysis, we performed multi-fluid numerical models of Alfvén waves in a nonuniform magnetic field configuration. One must bear in mind that the multifluid models used here are highly simplified: they do not include density stratification or gravity, nor do they capture the chromospheric dynamics, ionization/recombination, thermal conduction, or reflections of waves. Further work is obviously needed to investigate further the various effects that were ignored in this initial experiment.

However, in our results, the presence of different fluids (ionized and neutral fluids for various species) leads to both collisional and electric coupling. This, in turn, causes a (wave) phase offset between the various fluids and results in damping of the Alfvén waves due to collisions while propagating through the atmosphere. This coupling and damping leads to a positive ponderomotive acceleration, i.e., in the direction of the propagating wave. If the wave propagates upward, the ponderomotive force is upward, and for downward-propagating waves, the force is downward. The role of collisions is much stronger than the variations of the magnetic field (and thus the Alfvén speed) along the loop, which are meant to mimic a loop that expands or constricts with height. Our results suggest that the presence of multifluid damping in the chromosphere has a large potential to dominate any other type of ponderomotive forcing, and it may invalidate previous approaches that are based on other forms of the ponderomotive force. For example, the direction of the ponderomotive force in our simulations is different from what has been proposed in the recent literature (see below). Our results suggest that, if the ponderomotive force associated with Alfvén waves were the dominant mechanism driving the FIP effect, the Alfvén waves should propagate from the chromosphere to the corona. We note that the theory proposed by Laming (2017) is more easily reconciled with the observed FIP effect if one assumes that waves are generated in the corona and propagate into the chromosphere for closed loops. Apparently, this is not a strict requirement. However, it brings that theory in better alignment with the current observational evidence that indicates predominant upward propagation from the chromosphere into the corona (Okamoto & De Pontieu 2011) and a dominance of upward-propagating waves within the coronal volume at lower frequencies (Tomczyk et al. 2007).

We find that, in our models, the ponderomotive force increases with increasing wave amplitude or frequency of the Alfvén wave. We also find an increase in ponderomotive force in an environment in which the magnetic field strength increases in the direction of the wave propagation. We run cases assuming different approaches to ionizations with both SE populations and NEQ populations. The two scenarios are very different, leading to different ponderomotive accelerations and damping mechanisms. The SE case tends to damp the waves faster, due to the larger presence of neutrals.

Our results lead us to speculate about what this means for sunspots, which have much lower densities than other solar regions or phenomena. We speculate that this would lead to a reduced collisional coupling, such that our collisionless case might apply. If this were the case, it could potentially explain the inverse FIP effect that is sometimes seen in sunspots (Doschek & Warren 2016). However, this speculation needs

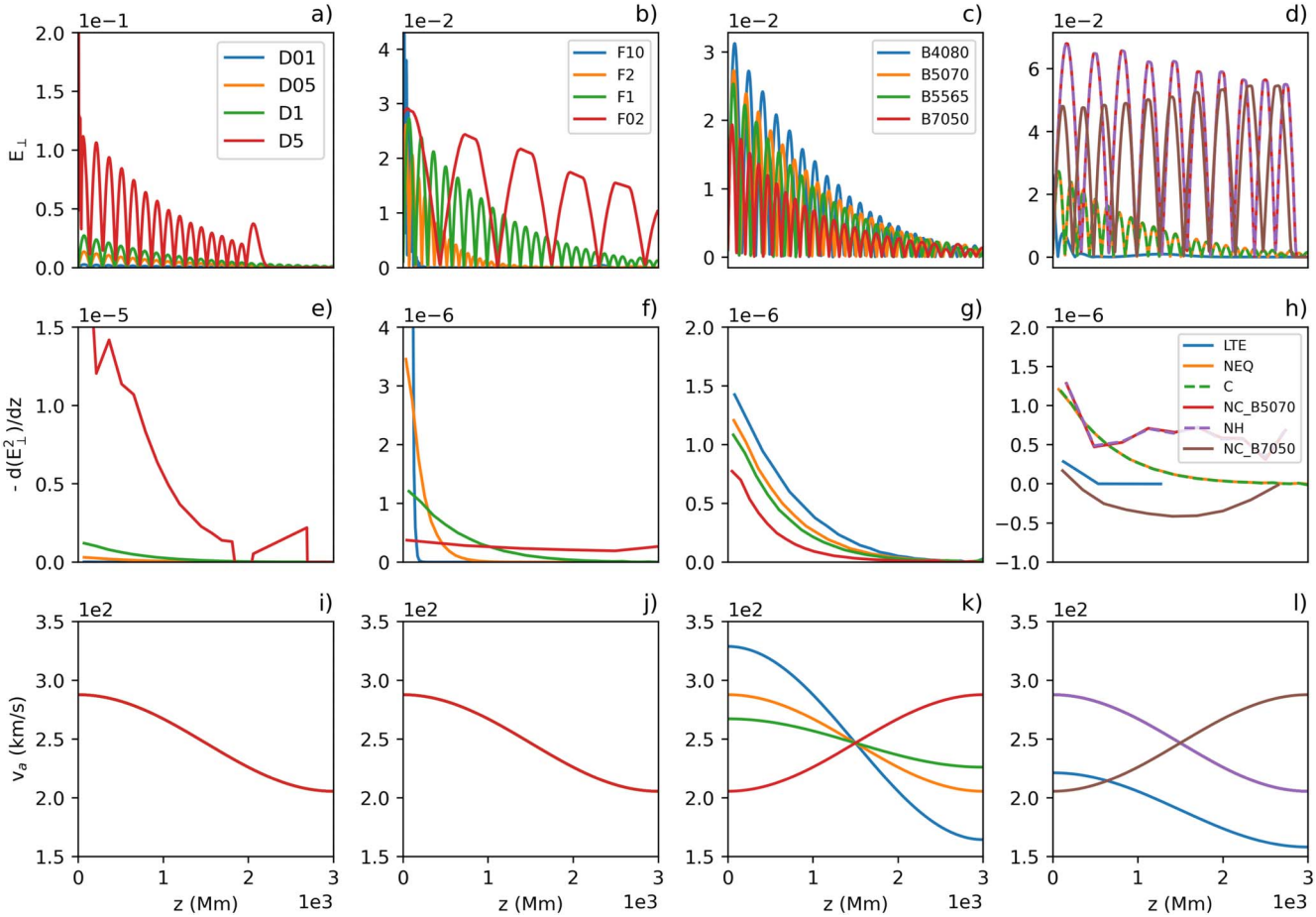

Figure 14. Electric field perpendicular to the magnetic field (top row), $-dE_\perp^2/dz$ (middle row), and Alfvén speed (bottom row), as a function of z-axis. We show this for a variety of simulations with varying amplitude, varying frequency of the Alfvén wave driver, variations of the guide magnetic field, and different physical assumptions, as shown, respectively, from left to right.

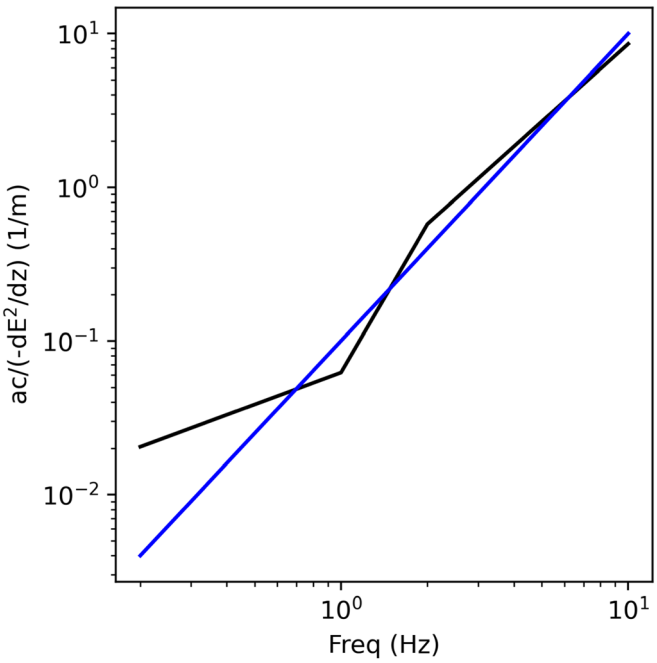

Figure 15. The ratio of the acceleration with $dE_\perp^2/dz$ for ionized helium as a function of frequency. The blue line follows a dependence of ω^2 and matches what is expected from the ponderomotive force associated with damping of Alfvén waves from ion–neutral damping (see text for details).

further investigation within the parameter range of a sunspot stratification.

We finish with the caveat that this first exploration of the relative motions and accelerations of ions with different first ionization potential is highly simplified and does not yet include various effects, including stratification. The latter has the potential to lead to larger spatial variations in the Alfvén speed than we considered here, which were only based on the varying guide field (not the density). At a minimum, this would mean that the conditions that we have called "expanding" or "constricting" loops (purely based on guide field changes) may well change meaning when stratification is included, given the expected change in sign of dv_A/ds. This is important to note because the ponderomotive force also depends on changes in v_A. In any case, large changes in Alfvén speed have the potential to change the ponderomotive force, e.g., through reflections from the transition region. Future numerical multi-fluid models that include more complexity are needed in order to move beyond the simplified analytical approaches of the current state-of-the-art FIP models and better understand how the ponderomotive force acts in the low solar atmosphere and can lead to fractionation.

It is clear from our results, however, that the presence of collisions in the partially ionized chromosphere introduces a ponderomotive force that, for the upper chromospheric thermodynamic and magnetic field conditions we have

considered here, may well dominate other types of ponderomotive force.

Our results indicate that collisional coupling between neutral hydrogen and neutral helium (and other neutral species) appears to dominate the damping of the high-frequency Alfvén waves we consider here. This could have a significant impact on coronal heating theories that depend on the generation of high-frequency Alfvén waves in the low solar atmosphere, e.g., magnetic reconnection, interactions between convection and magnetic field concentrations in the photosphere, etc. That is because this damping appears to be about six times higher than that of ion–neutral interactions for waves of 1 Hz, and it scales with the square of the wave frequency. Our results suggest that the upper chromosphere (including the spicules, which serve as a gateway to the corona) could act as a filter for high-frequency Alfvén waves. We speculate that this could play a role in explaining the apparent discrepancy in so-called AR outflow regions between the significant microturbulence at chromospheric heights and reduced nonthermal broadening in transition region lines (Testa et al. 2023). Perhaps the chromospheric turbulence is indeed caused by high-frequency Alfvén waves that are efficiently damped before they can reach transition region heights? More detailed and more realistic simulations of these effects are needed to determine whether this plays a role in the solar atmosphere.

We gratefully acknowledge support by NASA grants 80NSSC20K1272, 80NSSC21K0737, 80NSSC21K1684, and contract NNG09FA40C (IRIS) and the Grant Award 2149781 for funding opportunity NSF 21-577 Grand Challenges in Integrative Geospace Sciences: Advancing National Space Weather Expertise and Research toward Societal Resilience. Resources supporting this work were provided by the NASA High-End Computing (HEC) Program through the NASA Advanced Supercomputing (NAS) Division at Ames Research Center. The simulations have been run on Pleiades through the computing projects s1061, s2601, and s8305. This research is also supported by the Research Council of Norway through its Centres of Excellence scheme, project number 262622, and through grants of computing time from the Programme for Supercomputing. J.M.S. is very grateful to his family, and especially to his wife, for their support over many years that has allowed him to progress in his career, and to develop Ebysus, with the incredible help from the Ebysus team, that allowed the progress reported in this work.

ORCID iDs

Juan Martínez-Sykora https://orcid.org/0000-0002-0333-5717
Bart De Pontieu https://orcid.org/0000-0002-8370-952X
Viggo H. Hansteen https://orcid.org/0000-0003-0975-6659
Paola Testa https://orcid.org/0000-0002-0405-0668
Q. M. Wargnier https://orcid.org/0000-0002-8189-2922
Mikolaj Szydlarski https://orcid.org/0000-0002-9115-4448

References

Antolin, P., Schmit, D., Pereira, T. M. D., De Pontieu, B., & De Moortel, I. 2018, ApJ, 856, 44
Asplund, M., Grevesse, N., Sauval, A. J., & Scott, P. 2009, ARA&A, 47, 481
Avrett, E. H. 2007, in ASP Conf. Ser. 368, The Physics of Chromospheric Plasmas, ed. P. Heinzel, I. Dorotovič, & R. J. Rutten (San Francisco, CA: ASP), 81
Bale, S. D., Drake, J. F., McManus, M. D., et al. 2022, arXiv:2208.07932
Bale, S. D., Horbury, T. S., Velli, M., et al. 2021, ApJ, 923, 174
Ballester, J. L., Alexeev, I., Collados, M., et al. 2018, SSRv, 214, 58
Brooks, D. H., Ugarte-Urra, I., & Warren, H. P. 2015, NatCo, 6, 5947
Bruno, D., Catalfamo, C., Capitelli, M., et al. 2010, PhPl, 17, 112315
Carlsson, M., & Stein, R. F. 1992, ApJL, 397, L59
Dahlburg, R. B., Laming, J. M., Taylor, B. D., & Obenschain, K. 2016, ApJ, 831, 160
De Pontieu, B., Erdélyi, R., & James, S. P. 2004, Natur, 430, 536
De Pontieu, B., & Haerendel, G. 1998, A&A, 338, 729
De Pontieu, B., Martens, P. C. H., & Hudson, H. S. 2001, ApJ, 558, 859
De Pontieu, B., McIntosh, S. W., Carlsson, M., et al. 2007, Sci, 318, 1574
De Pontieu, B., Rouppe van der Voort, L., McIntosh, S. W., et al. 2014, Sci, 346, 1255732
Doschek, G. A., & Warren, H. P. 2016, ApJ, 825, 36
Fargette, N., Lavraud, B., Rouillard, A. P., et al. 2021, ApJ, 919, 96
Feldman, U. 1992, PhyS, 46, 202
Fox, N. J., Velli, M. C., Bale, S. D., et al. 2016, SSRv, 204, 7
Geiss, J., Gloeckler, G., & von Steiger, R. 1995, SSRv, 72, 49
Golding, T. P., Leenaarts, J., & Carlsson, M. 2016, ApJ, 817, 125
Gudiksen, B. V., Carlsson, M., Hansteen, V. H., et al. 2011, A&A, 531, A154
Haerendel, G. 1992, Natur, 360, 241
Hyman, J. M. 1979, in Advances in Computer Methods for Partial Differential Equations—III (Brussels: IMACS), 313
Kasper, J. C., Stevens, M. L., Korreck, K. E., et al. 2012, ApJ, 745, 162
Khomenko, E., & Cally, P. S. 2011, JPhCS, 271, 012042
Khomenko, E., Collados, M., Vitas, N., & González-Morales, P. A. 2021, RSPTA, 379, 20200176
Laming, J. M. 2004, ApJ, 614, 1063
Laming, J. M. 2015, LRSP, 12, 2
Laming, J. M. 2017, ApJ, 844, 153
Landi, E., & Testa, P. 2015, ApJ, 800, 110
Leenaarts, J., Carlsson, M., Hansteen, V., & Rutten, R. J. 2007, A&A, 473, 625
Lundin, R., & Guglielmi, A. 2006, SSRv, 127, 1
Lundin, R., & Hultqvist, B. 1989, JGR, 94, 6665
Maneva, Y. G., Ofman, L., & Viñas, A. 2015, A&A, 578, A85
Martínez-Gómez, D., Soler, R., & Terradas, J. 2015, A&A, 578, A104
Martínez-Sykora, J., De Pontieu, B., Hansteen, V. H., et al. 2017, Sci, 356, 1269
Martínez-Sykora, J., Leenaarts, J., De Pontieu, B., et al. 2020, ApJ, 889, 95
McIntosh, S. W., & De Pontieu, B. 2009, ApJ, 707, 524
McIntosh, S. W., de Pontieu, B., Carlsson, M., et al. 2011, Natur, 475, 477
Meyer, J.-P. 1985, ApJS, 57, 151
Müller, D., St., Cyr, O. C., Zouganelis, I., et al. 2020, A&A, 642, A1
Nóbrega-Siverio, D., Moreno-Insertis, F., Martínez-Sykora, J., Carlsson, M., & Szydlarski, M. 2020, A&A, 633, A66
Ofman, L., Davila, J. M., Nakariakov, V. M., & ViñAs, A. F. 2005, JGRA, 110, A09102
Okamoto, T. J., & De Pontieu, B. 2011, ApJL, 736, L24
Pereira, T. M. D., De Pontieu, B., Carlsson, M., et al. 2014, ApJL, 792, L15
Popescu Braileanu, B., Lukin, V. S., Khomenko, E., & de Vicente, Á. 2019, A&A, 627, A25
Przybylski, D., Cameron, R., Solanki, S. K., et al. 2022, A&A, 664, A91
Rempel, M., & Przybylski, D. 2021, ApJ, 923, 79
Soler, R., Andries, J., & Goossens, M. 2012, A&A, 537, A84
Song, P., & Vasyliūnas, V. M. 2011, JGRA, 116, A09104
Testa, P. 2010, SSRv, 157, 37
Testa, P., De Pontieu, B., & Hansteen, V. 2016, ApJ, 827, 99
Testa, P., Martinez-Sykora, J., & De Pontieu, B. 2023, ApJ, 944, 117
Testa, P., Saar, S. H., & Drake, J. J. 2015, RSPTA, 373, 20140259
Tomczyk, S., McIntosh, S. W., Keil, S. L., et al. 2007, Sci, 317, 1192
Wargnier, Q. M., Martínez-Sykora, J., Hansteen, V. H., & De Pontieu, B. 2022, ApJ, 933, 205
Wargnier, Q. M., Martinez-Sykora, J., Hansteen, V. H., & De Pontieu, B. 2023, ApJ, 946, 115
Whitelam, S., Ashbourn, J. M. A., Bingham, R., Shukla, P. K., & Spicer, D. S. 2002, SoPh, 211, 199
Woolley, T., Matteini, L., McManus, M. D., et al. 2021, MNRAS, 508, 236
Zaqarashvili, T. V., Khodachenko, M. L., & Rucker, H. O. 2011, A&A, 534, A93